applied sciences

MDPI

Article

A Block-Coupled Finite Volume Method for Incompressible Hyperelastic Solids

Anja Horvat [1], Philipp Milović [2], Igor Karšaj [1] and Željko Tuković [1,*]

[1] Faculty of Mechanical Engineering and Naval Architecture, University of Zagreb, 10000 Zagreb, Croatia; anja.horvat@fsb.unizg.hr (A.H.); igor.karsaj@fsb.unizg.hr (I.K.)
[2] School of Medicine, University of Zagreb, 10000 Zagreb, Croatia; milovic.ph@gmail.com
* Correspondence: zeljko.tukovic@fsb.unizg.hr

Abstract

This work introduces a block-coupled finite volume method for simulating the large-strain deformation of incompressible hyperelastic solids. Conventional displacement-based finite-volume solvers for incompressible materials often exhibit stability and convergence issues, particularly on unstructured meshes and in finite-strain regimes typical of biological tissues. To address these issues, a mixed displacement–pressure formulation is adopted and solved using a block-coupled strategy, enabling simultaneous solution of displacement and pressure increments. This eliminates the need for under-relaxation and improves robustness compared to segregated approaches. The method incorporates several enhancements, including temporally consistent Rhie–Chow interpolation, accurate treatment of traction boundary conditions, and compatibility with a wide range of constitutive models, from linear elasticity to advanced hyperelastic laws such as Holzapfel–Gasser–Ogden and Guccione. Implemented within the solids4Foam toolbox for OpenFOAM, the solver is validated against analytical and finite-element benchmarks across diverse test cases, including uniaxial extension, simple shear, pressurised cylinders, arterial wall, and idealised ventricle inflation. Results demonstrate second-order spatial and temporal accuracy, excellent agreement with reference solutions, and reliable performance in three-dimensional scenarios. The proposed approach establishes a robust foundation for fluid–structure interaction simulations in vascular and soft tissue biomechanics.

Keywords: cell-centred finite volume method; hyperelasticity; incompressibility; block-coupled; solid mechanics; soft tissue; vascular mechanics; OpenFOAM; solids4Foam

check for updates

Academic Editor: Lei Wang

Received: 25 September 2025
Revised: 11 November 2025
Accepted: 12 November 2025
Published: 28 November 2025

Citation: Horvat, A.; Milović, P.; Karšaj, I.; Tuković, Ž. A Block-Coupled Finite Volume Method for Incompressible Hyperelastic Solids. *Appl. Sci.* **2025**, *15*, 12660. https://doi.org/10.3390/app152312660

Copyright: © 2025 by the authors. Licensee MDPI, Basel, Switzerland. This article is an open access article distributed under the terms and conditions of the Creative Commons Attribution (CC BY) license (https://creativecommons.org/licenses/by/4.0/).

1. Introduction

A considerable range of engineering applications involves materials capable of sustaining large-strain elastic deformations while exhibiting incompressible or nearly incompressible mechanical behaviour. Rubber is a canonical example, capable of undergoing substantial stretching or bending without an appreciable change in volume. Many soft biological tissues, including muscle, skin, and arterial walls, are commonly idealized as incompressible because of their high water content, which effectively suppresses volumetric change. Hydrogels and silicone gels exhibit similar characteristics, and many engineering elastomers (such as polyurethane and silicone rubber) are also modeled as incompressible in mechanical analyses.

It is well established that numerical stress analysis of solids approaching the incompressible limit presents significant challenges, particularly when a displacement-based

formulation is employed. In particular, fully integrated, displacement-based lower-order finite elements often exhibit volumetric locking, a phenomenon frequently accompanied by pressure oscillations. Both volumetric locking and pressure oscillations have been extensively studied, leading to the development of various strategies aimed at mitigating these issues. The most widely used approach to prevent volumetric locking within the Finite Element (FE) framework is the mixed displacement-pressure formulation [1]. This method introduces pressure as an independent variable alongside displacement, allowing the problem to be formulated in a way that enforces the incompressibility constraint without locking.

In Computational Solid Mechanics (CSM), the FE method remains the most widely used approach. However, the Finite Volume (FV) method—long established in Computational Fluid Dynamics—has been steadily expanding its reach into CSM. Its growing popularity is due to its conceptual simplicity and strong conservation properties. Over the years, the FV method has been applied to a broad spectrum of CSM problems, emerging in several distinct variants based on different control-volume arrangements, most notably the cell-centred and vertex-centred schemes. A comprehensive review is provided in [2].

Only a limited number of FV methods have been proposed for incompressible materials [3]. The present study builds on the work of Professor I. Demirdžić and collaborators [4–6], who employed a mixed displacement–pressure formulation to prevent volumetric locking. The mathematical model consists of the momentum equation, the mass conservation equation (incompressibility condition), and the constitutive equation. Spatial discretisation is performed using a cell-centred FV method applied to meshes with control volumes of completely arbitrary topology. The resulting set of coupled linear algebraic equations is solved using a segregated procedure incorporating a SIMPLE-based algorithm [7], which ensures the required pressure–displacement coupling through the use of Rhie–Chow interpolation [8] to evaluate displacement at the control volume faces. In the present study, the following improvements to the above models are proposed:

1. Block-coupled solution procedure: Instead of using a segregated solution procedure, in which displacement increment components and the pressure increment are solved separately, a block-coupled system of linear algebraic equations (representing the discretised momentum and pressure increment equations) is solved for displacement and pressure increments simultaneously. This leads to a more robust and efficient solution process, as there is no need to apply user-defined under-relaxation to the displacement and pressure increments. The proposed block-coupled solution procedure is based on the procedure proposed by Professor M. Darwish and collaborators [9,10] for the solution of laminar incompressible flow problems on collocated unstructured FV grids. Later, a similar algorithm was implemented [11,12] in the OpenFOAM framework [13], which serves as the starting point for the implementation of an algorithm for solving incompressible elastic/hyperelastic solid deformations in this work.
2. Temporal discretisation: Emphasis is placed on the temporal accuracy of the model, as the ultimate objective is its application to fluid–structure interaction simulations in vascular flows. Four commonly used temporal discretisation schemes are implemented and tested, each incorporating a temporally consistent Rhie–Chow interpolation [14].
3. Improved treatment of traction boundaries—Along the portions of the discretised spatial domain boundary where traction is specified, the displacement increment is calculated using the cell-face normal component obtained from the solution of the continuity (pressure increment) equation, while the remaining components are reconstructed using the selected constitutive equation. This approach provides substantially higher accuracy at the traction boundaries compared with the second-order extrapolation used in [4].

4. Extended material applicability: The proposed FV solver is applicable to both linear elastic bodies and nonlinear hyperelastic materials described by arbitrary constitutive equations, with emphasis on constitutive relations used for modelling arterial walls and heart tissue (for example, Holzapfel-Gasser-Ogden (HGO) model [15] and Guccione model [16]).

The proposed FV solver for incompressible elastic/hyperelastic bodies is implemented within the solids4Foam toolbox [17,18], which extends the OpenFOAM framework to allow the straightforward implementation of advanced solid mechanics and fluid–structure interaction (FSI) procedures. In this way, the proposed FV solver provides the foundation for developing a self-contained FSI solver for vascular flows in the next step.

In the next section, the governing equations and constitutive relations are presented, followed by a brief description of the FV discretisation procedure and the solution algorithm. Finally, the capabilities of the method are demonstrated through a series of test cases.

2. Mathematical Model

The deformation of an arbitrary body of volume Ω, bounded by a surface Γ, is governed by the law of conservation of linear momentum, which can be expressed in the following integral form:

$$\frac{\partial}{\partial t}\int_{\Omega}\rho\frac{\partial \boldsymbol{u}}{\partial t}\,\mathrm{d}\Omega = \int_{\Gamma}\boldsymbol{n}\cdot\boldsymbol{\sigma}\,\mathrm{d}\Gamma, \tag{1}$$

where t is time, ρ is density, $\boldsymbol{u}$ is the displacement vector, $\boldsymbol{n}$ is the outward-pointing normal vector of the surface Γ, $\boldsymbol{\sigma}$ is the Cauchy stress tensor, and the body force is omitted for clarity. Equation (1) is integrated over the body in the deformed configuration. In this study, the alternative formulation of the linear momentum conservation law is used, where integration is performed over the body in the initial undeformed configuration:

$$\frac{\partial}{\partial t}\int_{\Omega^0}\rho^0\frac{\partial \boldsymbol{u}}{\partial t}\,\mathrm{d}\Omega^0 = \int_{\Gamma^0}\left(J\boldsymbol{F}^{-\mathrm{T}}\cdot\boldsymbol{n}^0\right)\cdot\boldsymbol{\sigma}\,\mathrm{d}\Gamma^0, \tag{2}$$

where the superscript 0 indicates that a quantity refers to the initial configuration ($t = 0$ s); for example, Ω^0 denotes the initial undeformed volume bounded by the corresponding initial undeformed surface Γ^0. In the surface integral on the right-hand side of Equation (2), Nanson's formula is used to transform the elementary area vector from the initial to the current configuration, where $\boldsymbol{F} = \boldsymbol{I} + (\nabla_0\boldsymbol{u})^{\mathrm{T}}$ is the deformation gradient tensor, $J = \det\boldsymbol{F}$ is the Jacobian of the deformation gradient, $\boldsymbol{I}$ is the unit (identity) tensor, and ∇_0 denotes the gradient operator with respect to the initial configuration (When there is no difference between initial and current configuration, like in the case of linear elasticity, the subscript next to the ∇ operator is omitted.). To close the model, it is necessary to specify the constitutive relation between the Cauchy stress tensor $\boldsymbol{\sigma}$ and the displacement vector $\boldsymbol{u}$, which is presented in the following section.

2.1. Constitutive Equations

The ultimate goal of this study is to develop a finite-volume solver for the simulation of large-strain dynamic deformation in elastic bodies composed of incompressible material, with a particular focus on applications in vascular system modelling. The solver currently handles incompressible elasticity/hyperelasticity but can be readily extended to compressible materials, following the same numerical approach as in [19]. Moreover, it consistently recovers the limit of linear elasticity, corresponding to small strains and rotations.

Constitutive relation for an isotropic linear elastic solid valid only under the small strain and small rotation assumption is Hook's law:

$$\boldsymbol{\sigma} = 2\mu\boldsymbol{\epsilon} + \lambda(\nabla \cdot \boldsymbol{u})\boldsymbol{I}, \tag{3}$$

where μ and λ are Láme coefficients and ε is the linear strain tensor:

$$\boldsymbol{\epsilon} = \frac{1}{2}\left[\nabla \boldsymbol{u} + (\nabla \boldsymbol{u})^{\mathrm{T}}\right]. \tag{4}$$

The Láme coefficients μ and λ as well as the bulk elasticity modulus K can be defined through Young's elasticity modulus E and Poisson's ratio ν by the following relations:

$$\mu = \frac{E}{2(1+\nu)}, \quad \lambda = \frac{E\nu}{(1+\nu)(1-2\nu)}, \quad K = \frac{E}{3(1-2\nu)}. \tag{5}$$

It can be observed that Equation (3) is not well defined in the incompressible limit since for $\nu \to \frac{1}{2}$, $\lambda \to \infty$ and $\nabla \cdot \boldsymbol{u} \to 0$. To avoid this issue, pressure can be introduced as an additional independent variable, defined by the following equation:

$$p = -K\nabla \cdot \boldsymbol{u}. \tag{6}$$

Taking into account Equation (6), Hook's law (3) can be rewritten in a mixed (pressure-displacement) formulation as follows:

$$\boldsymbol{\sigma} = 2\mu\boldsymbol{\epsilon} - \frac{\lambda}{K}p\boldsymbol{I}, \tag{7}$$

$$\nabla \cdot \boldsymbol{u} = -\frac{p}{K}, \tag{8}$$

In the limit of incompressibility $\nu \to \frac{1}{2}$, $\lambda/K \to 1$ and $1/K \to 0$, hence Equations (7) and (8) reduce to the following:

$$\boldsymbol{\sigma} = 2\mu\boldsymbol{\epsilon} - p\boldsymbol{I}, \tag{9}$$

$$\nabla \cdot \boldsymbol{u} = 0, \tag{10}$$

which represents a well-defined constitutive relation for an incompressible linear elastic material. Equation (10) represents the continuity equation for an incompressible material and is also referred to as the incompressibility condition.

Nonlinear elastic behaviour can be represented by various hyperelastic models. Here, the Neo-Hookean law is used as a reference, and the solver is structured to easily incorporate alternative formulations.

Deformation of a compressible Neo-Hookean solid (Ogden variant) can be described by the following constitutive relation in the mixed (pressure-displacement) formulation:

$$\boldsymbol{\sigma} = \frac{\mu}{J}(\mathbf{B} - \boldsymbol{I}) - \frac{\lambda}{K}p\boldsymbol{I}, \tag{11}$$

where $\boldsymbol{B} = \boldsymbol{F} \cdot \boldsymbol{F}^{\mathrm{T}}$ is the left Cauchy-Green tensor. A mixed formulation is again used in order to facilitate the modelling of incompressible materials. In the limit of incompressibility Equation (11) reduces to the following:

$$\boldsymbol{\sigma} = \mu(\mathbf{B} - \boldsymbol{I}) - p\boldsymbol{I}. \tag{12}$$

The constitutive relations described above are expressed in terms of the total displacement $\boldsymbol{u}$, which is consistent with the total displacement formulation of the linear momentum conservation law (2). In this study, incremental displacement formulation of the linear momentum conservation law is applied since this approach can have a positive effect on the efficiency and stability of a numerical procedure. Hence, it is necessary to express stress increment in terms of displacement increment $\delta\boldsymbol{u} = \boldsymbol{u} - \boldsymbol{u}^n$, where superscript n refers to the known quantities from the previous time step (Discretisation of temporal solution domain will be described later, but one can define the previous time instance here $t^n = n\Delta t$, while the current time instance is $t^{n+1} = (n+1)\Delta t$, where Δt is the time-step size.). Accordingly, one can express the Cauchy stress increment tensor in terms of displacement increment and pressure increments for the incompressible Hook's law as follows:

$$\delta\boldsymbol{\sigma} = \boldsymbol{\sigma} - \boldsymbol{\sigma}^n = \mu\left[\nabla\delta\boldsymbol{u} + (\nabla\delta\boldsymbol{u})^{\mathrm{T}}\right] - \delta p\,\boldsymbol{I}, \tag{13}$$

where δp is the pressure increment. Cauchy stress increment for an incompressible Neo-Hookean solid reads as follows:

$$\delta\boldsymbol{\sigma} = \mu\left[\boldsymbol{F}^n \cdot (\nabla_0\delta\boldsymbol{u}) + (\nabla_0\delta\boldsymbol{u})^{\mathrm{T}} \cdot (\boldsymbol{F}^n)^{\mathrm{T}}\right] - \delta p\,\boldsymbol{I}, \tag{14}$$

where the nonlinear quadratic term $(\nabla_0\delta\boldsymbol{u})^{\mathrm{T}} \cdot \nabla_0\delta\boldsymbol{u}$ is omitted. One can note that (14) reduces to expression (13) if the assumption of linear elasticity is satisfied ($\boldsymbol{F} \approx \boldsymbol{I}$).

As stated earlier in this section, the Neo-Hookean material model is used as the foundation for the hyperelastic variant of the proposed FV solver, while the application of alternative hyperelastic models is implemented through the traction correction term, as will be shown in the next section. Among the available alternative hyperelastic models, the incompressible HGO model [15] and the incompressible Guccione model [16] are considered in this study. The application of more advanced hyperelastic models, such as those based on the novel hyperbolic-sine strain measure [20–22], will be considered in future work.

2.2. Resulting Set of Equations for Incompressible Solid

The resulting set of governing equations, which are solved numerically, consists of the linear momentum conservation law and the mass conservation law (incompressibility conditions). As mentioned earlier, in order to enhance the numerical efficiency, the incremental formulation of the conservation laws is used.

Incremental formulation of the conservation law for total linear momentum reads as follows:

$$\frac{\partial}{\partial t}\int_{\Omega^0} \rho^0 \frac{\partial(\delta\boldsymbol{u} + \boldsymbol{u}^n)}{\partial t}\,\mathrm{d}\Omega^0 = \int_{\Gamma^0}\left[(\boldsymbol{F}^n)^{-\mathrm{T}} \cdot \boldsymbol{n}^0\right] \cdot \left[\delta\boldsymbol{\sigma} + \boldsymbol{\sigma}^n\right]\,\mathrm{d}\Gamma^0. \tag{15}$$

By expressing the Cauchy stress increment $\delta\boldsymbol{\sigma}$ in the above equation in terms of the unknown displacement increment $\delta\boldsymbol{u}$ and pressure increment δp via the incremental constitutive relation (14), the balance of linear momentum takes the following final form:

$$\frac{\partial}{\partial t}\int_{\Omega^0} \rho^0 \frac{\partial(\delta\boldsymbol{u} + \boldsymbol{u}^n)}{\partial t}\,\mathrm{d}\Omega^0 = \int_{\Gamma^0} \delta\boldsymbol{T}\,\mathrm{d}\Gamma^0 + \int_{\Gamma^0} \boldsymbol{T}^n\,\mathrm{d}\Gamma^0, \tag{16}$$

where the traction from the previous time instance $\boldsymbol{T}^n$ and the traction increment $\delta\boldsymbol{T}$ are defined as follows:

$$\boldsymbol{T}^n = \left[(\boldsymbol{F}^n)^{-\mathrm{T}} \cdot \boldsymbol{n}^0\right] \cdot \boldsymbol{\sigma}^n, \tag{17}$$

$$\delta \boldsymbol{T} = \left[(\boldsymbol{F}^{\mathrm{n}})^{-\mathrm{T}} \cdot \boldsymbol{n}^0 \right] \cdot \delta \boldsymbol{\sigma} = \mu_{\mathrm{eff}} \left\{ (\boldsymbol{n}^0 \cdot \nabla_0 \delta \boldsymbol{u}) + \left[\boldsymbol{n}^0 \cdot (\nabla_0 \delta \boldsymbol{u})^{\mathrm{T}} \right] \right\} - \\ - \left[(\boldsymbol{F}^n)^{-\mathrm{T}} \cdot \boldsymbol{n}^0 \right] \delta p. \tag{18}$$

Equation (16), with tractions defined by Equations (17) and (18), is not exact even for the Neo-Hookean model because, in its derivation, the current deformation gradient is approximated by that from the previous time step ($\boldsymbol{F} \approx \boldsymbol{F}^n$) and the quadratic term in the incremental constitutive relation (14) is neglected. In addition, the effective or instantaneous shear modulus μ_{eff} is used in Equation (18) instead of the shear modulus μ of the Neo-Hookean model (In the Neo-Hookean model, the shear modulus remains constant. In contrast, for example, in the HGO model, the shear modulus coincides with that of the Neo-Hookean model in the undeformed state, but it evolves with deformation of the elastic body). The procedure used to calculate the approximate value of instantaneous shear modulus is described in Appendix A. To compensate for these approximations, the following traction-correction term is added to the right-hand side of Equation (16):

$$\boldsymbol{T}' = \left[(\boldsymbol{F}^*)^{-\mathrm{T}} \cdot \boldsymbol{n}^0 \right] \cdot \boldsymbol{\sigma}(\boldsymbol{F}^*, p^*) - (\delta \boldsymbol{T}^* + \boldsymbol{T}^n), \tag{19}$$

where superscript $*$ represents quantities obtained in the previous iteration of the iterative solution procedure (It is usual practice to use an iterative solution procedure to solve non-linear problems in computational mechanics. Even in the case of linear problems, iterative solution procedures have to be used in the framework of the FV method since different kinds of corrections related to preservation of accuracy are applied using different correction approaches.) In such a way, the Cauchy stress tensor $\boldsymbol{\sigma}(\boldsymbol{F}^*, p^*)$ is evaluated using the selected hyperelastic constitutive model based on the values of the unknown displacement (displacement gradient) and pressure fields from the previous iteration. In the case of linear-elastic material, the traction correction term (19) vanishes, and Equations (17) and (18) simplify by taking into account that $\boldsymbol{F}^n = \boldsymbol{I}$.

Taking into account the traction correction term defined by Equation (19), the final form of the linear momentum conservation equation reads as follows:

$$\frac{\partial}{\partial t} \int_{\Omega^0} \rho^0 \frac{\partial (\delta \boldsymbol{u} + \boldsymbol{u}^n)}{\partial t} \, \mathrm{d}\Omega^0 = \int_{\Gamma^0} \delta \boldsymbol{T} \, \mathrm{d}\Gamma^0 + \int_{\Gamma^0} \boldsymbol{T}^n \, \mathrm{d}\Gamma^0 + \int_{\Gamma^0} \boldsymbol{T}' \, \mathrm{d}\Gamma^0. \tag{20}$$

The accuracy of the above equation must be assessed in the context of the iterative solution procedure. In each iteration, the first and last terms on the right-hand side are computed using the solution from the previous iteration; only once the solution has converged does the right-hand side of Equation (20) approach the correct force integrated over the control-volume boundary.

In order to close the model, which consists of two unknown fields (displacement increment and pressure increment), it is necessary to take into account Equation (10) transformed into incremental integral form:

$$\int_{\Gamma} \boldsymbol{n} \cdot \delta \boldsymbol{u} \, \mathrm{d}\Gamma = 0, \tag{21}$$

where integration is performed over the volume of the body in the current (deformed) configuration. Equation (21) does not represent the governing equation for pressure increment, but an additional constraint for displacement increment. The so-called pressure increment equation will be derived later by combining discretised counterparts of Equations (20) and (21).

2.3. Initial and Boundary Conditions

To complete the mathematical model, initial and boundary conditions must be specified. For the numerical solution of transient problems, it is necessary to prescribe the displacement and velocity at the initial time and at all computational points of the spatial solution domain. Boundary conditions must be specified at all times along all spatial domain boundaries. The most common boundary conditions in solid mechanics are prescribed displacement (Dirichlet) and prescribed traction (Neumann). These conditions may be constant or time-dependent.

3. Numerical Model

The mathematical model is discretised in space using a second-order accurate collocated (cell-centred) unstructured FV method, while numerical integration in time is performed using various implicit schemes. The discretisation procedure is divided into two parts: discretisation of the solution domain and discretisation of the governing equations.

3.1. Solution Domain Discretisation

The solution domain comprises the temporal solution domain (i.e., the total solution time) and the spatial solution domain. The total solution time is divided into a finite number of time steps Δt, and the equations are solved in a time-marching manner. In the unstructured FV discretisation, the spatial solution domain is partitioned into a finite number of convex polyhedral control volumes (CVs) or cells, each bounded by convex polygonal faces. The cells do not overlap and completely fill the spatial domain. Figure 1 illustrates a simple polyhedral control volume Ω_P around the computational point P located at its centroid, the face f, the face area Γ_f, the unit normal vector $\boldsymbol{n}_f$ to the face, and the centroid N of the neighbouring CV sharing the face f. In the general case, the interpolation point f' does not coincide with the face centre point f , and the distance between them is defined by the skewness correction vector $\mathbf{k}_f$. The geometry of a CV is fully determined by the positions of its vertices.

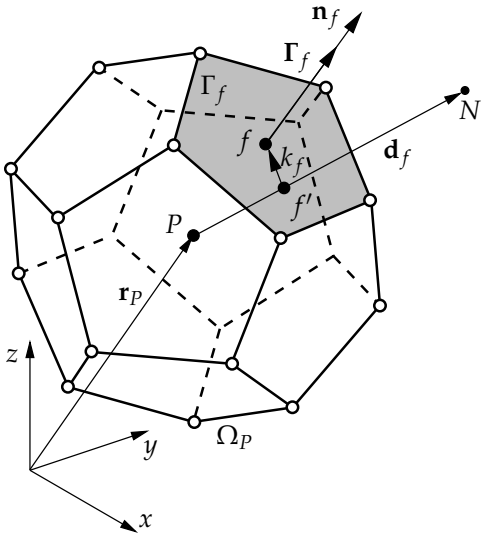

Figure 1. An example of a polyhedral control volume (cell) P with its neighbour cell centre N and the shared face f [23]. The face f is coloured gray.

3.2. Governing Equations Discretisation

The second-order FV discretisation of an integral conservation equation transforms surface integrals into sums of face integrals and approximates both the surface and volume integrals to second-order accuracy using the midpoint rule. Temporal discretisation is

carried out by numerical integration of the governing equation in time from the old time instance t^n to the new time instance $t^{n+1} = t^n + \Delta t$.

3.2.1. Momentum Equation Discretisation

The spatially discretised momentum Equation (20) for the control volume Ω_P can be written as follows:

$$\rho_P^0 \frac{\partial}{\partial t}\left[\frac{\partial(\delta \boldsymbol{u}_P + \boldsymbol{u}_P^n)}{\partial t}\right]\Omega_P^0 = \underbrace{\sum_f \delta \boldsymbol{T}_f \boldsymbol{\Gamma}_f^0}_{\text{implicit}} + \underbrace{\sum_f \boldsymbol{T}_f^n \boldsymbol{\Gamma}_f^0 + \sum_f \boldsymbol{T}_f' \boldsymbol{\Gamma}_f^0}_{\text{explicit}}, \tag{22}$$

where the subscripts P and f denote the cell-centre and face-centre values, respectively, with the summation taken over all faces bounding cell P. In Equation (22), the first term on the right-hand side is treated implicitly after discretisation, whereas the last two terms are explicit and evaluated using displacement and pressure fields (or their increments) from the previous time step or iteration.

The traction increment $\delta \boldsymbol{T}_f$ in the implicit term on the right-hand side of Equation (22) is obtained by discretising Equation (18) at the centers of internal faces as follows:

$$\begin{aligned}\delta \boldsymbol{T}_f = (\mu_{\text{eff}})_f (\boldsymbol{n}^0 \cdot \nabla_0 \delta \boldsymbol{u})_f + (\mu_{\text{eff}})_f \left[\boldsymbol{n}^0 \cdot \nabla_0 (\delta \boldsymbol{u} \cdot \boldsymbol{n}^0 \boldsymbol{n}^0)\right]_f + \\ + (\mu_{\text{eff}})_f \left[\nabla_{0t} (\delta \boldsymbol{u} \cdot \boldsymbol{n}^0)\right]_f^* - \left[(\boldsymbol{F}_f^n)^{-\mathrm{T}} \cdot \boldsymbol{n}_f^0\right] \delta p_f,\end{aligned} \tag{23}$$

where the second and third terms on the right-hand side are obtained by decomposition of the gradient transpose term as follows:

$$\boldsymbol{n}^0 \cdot (\nabla_0 \delta \boldsymbol{u})^{\mathrm{T}} = \nabla_0 (\delta \boldsymbol{u} \cdot \boldsymbol{n}^0) = \boldsymbol{n}^0 \cdot \nabla_0 (\delta \boldsymbol{u} \cdot \boldsymbol{n}^0 \boldsymbol{n}^0) + \nabla_{0t} (\delta \boldsymbol{u} \cdot \boldsymbol{n}^0), \tag{24}$$

where $\nabla_{0t} = (\boldsymbol{I} - \boldsymbol{n}^0 \boldsymbol{n}^0) \cdot \nabla_0$ is the tangential gradient operator.

The face normal derivative of displacement increment in Equation (23) is discretised using the central scheme with non-orthogonal and skewness corrections as follows (see Figure 1):

$$(\boldsymbol{n}^0 \cdot \nabla_0 \delta \boldsymbol{u})_f = \frac{\delta \boldsymbol{u}_N - \delta \boldsymbol{u}_P}{d_{f,n}^0} + \frac{\mathbf{k}_N^0 \cdot (\nabla_0 \delta \boldsymbol{u})_N^* - \mathbf{k}_P^0 \cdot (\nabla_0 \delta \boldsymbol{u})_P^*}{d_{f,n}^0}, \tag{25}$$

where $d_{f,n}^0 = \boldsymbol{n}_f^0 \cdot \mathbf{d}_f^0$, $\mathbf{k}_P^0 = (\boldsymbol{I} - \boldsymbol{n}_f^0 \boldsymbol{n}_f^0) \cdot (\mathbf{r}_f^0 - \mathbf{r}_P^0)$ and $\mathbf{k}_N^0 = (\boldsymbol{I} - \boldsymbol{n}_f^0 \boldsymbol{n}_f^0) \cdot (\mathbf{r}_N^0 - \mathbf{r}_f^0)$. The first term on the right-hand side of Equation (25) is treated implicitly, while the correction term is treated explicitly. The discretisation scheme in Equation (25) is also applied to the face-normal derivative of the normal displacement increment, $[\boldsymbol{n}^0 \cdot \nabla_0 (\delta \boldsymbol{u} \cdot \boldsymbol{n}^0 \boldsymbol{n}^0)]_f$, where $\delta \boldsymbol{u}$ is replaced by its normal component, $\delta \boldsymbol{u} \cdot (\boldsymbol{n}^0 \boldsymbol{n}^0)$.

The face-centre value of the pressure increment δp_f in Equation (23) is calculated using linear interpolation of the neighbouring cell-centre values with the skewness correction:

$$\delta p_f = {}^0\overline{\overline{(\delta p_P)}}_f = {}^0\overline{(\delta p_P)}_f + \mathbf{k}_f^0 \cdot {}^0\overline{(\nabla_0 \delta p)}_f^*, \tag{26}$$

where $\mathbf{k}_f^0$ is the skewness correction vector between the cell-face interpolation point f' and the cell-face centre f, as illustrated in Figure 1. The linear interpolation procedure is then defined as follows:

$${}^0\overline{(\delta p_P)}_f = g_x^0 \delta p_P + (1 - g_x^0) \delta p_N, \tag{27}$$

Here, $g_x^0 = (\overline{f'N})^0 / (\overline{PN})^0$ is the interpolation factor (see Figure 1), and the obtained cell-face value corresponds to the value at the interpolation point f', which coincides with

the cell-face centre f for a mesh without skewness (In the remainder of this manuscript, the operator ${}^{0}\overline{(\circ)}_f$ denotes the calculation of cell-face values by linear interpolation of neighbouring cell-centre values without skewness correction, as defined in Equation (27), whereas the operator ${}^{0}\overline{\overline{(\circ)}}_f$ denotes the linear interpolation with skewness correction, as defined in Equation (26). Left-hand side superscript in the above operators indicates mesh configuration on which linear interpolation is performed and on which gradient for skewness correction is calculated.). The skewness correction term in Equation (26) is treated explicitly, meaning it is evaluated using the pressure increment field obtained from the previous iteration.

The fully discretised momentum equation is obtained by numerical integration of Equation (22) over the time interval $[t^n, t^{n+1}]$, where approximation of the time integrals is carried out using implicit two-level Euler scheme, Crank-Nicolson (trapezoidal) scheme, and implicit three-level backward scheme. Backward and trapezoidal schemes are also combined to form the so-called composite scheme proposed by Bathe [24]. The fully discretised momentum equation obtained by applying the above-listed temporal discretisation schemes reads as follows:

- Euler scheme

$$\rho_P^0 \frac{\boldsymbol{v}_P^{n+1} - \boldsymbol{v}_P^n}{\Delta t} \Omega_P^0 = \sum_f \delta \boldsymbol{T}_f^{n+1} \Gamma_f^0 + \sum_f \boldsymbol{T}_f^n \Gamma_f^0 + \sum_f (\boldsymbol{T}'_f)^* \Gamma_f^0, \tag{28}$$

$$\boldsymbol{v}_P^{n+1} = \frac{\boldsymbol{u}_P^{n+1} - \boldsymbol{u}_P^n}{\Delta t} = \frac{\delta \boldsymbol{u}_P^{n+1}}{\Delta t}, \tag{29}$$

- Crank-Nicolson scheme

$$\begin{aligned} \rho_P^0 \frac{\boldsymbol{v}_P^{n+1} - \boldsymbol{v}_P^n}{\Delta t} \Omega_P^0 = & \frac{1}{2} \sum_f \delta \boldsymbol{T}_f^{n+1} \Gamma_f^0 + \frac{1}{2} \sum_f \boldsymbol{T}_f^n \Gamma_f^0 + \\ & \frac{1}{2} \sum_f (\boldsymbol{T}'_f)^* \Gamma_f^0 + \frac{1}{2} \sum_f \boldsymbol{T}_f^n \Gamma_f^0, \end{aligned} \tag{30}$$

$$\boldsymbol{v}_P^{n+1} = 2 \frac{\boldsymbol{u}_P^{n+1} - \boldsymbol{u}_P^n}{\Delta t} - \boldsymbol{v}_P^n = 2 \frac{\delta \boldsymbol{u}_P^{n+1}}{\Delta t} - \boldsymbol{v}_P^n, \tag{31}$$

- backward scheme

$$\begin{aligned} \rho_P^0 \frac{3\boldsymbol{v}_P^{n+1} - 4\boldsymbol{v}_P^n + \boldsymbol{v}_P^{n-1}}{2\Delta t} \Omega_P = & \\ \sum_f \delta \boldsymbol{T}_f^{n+1} \Gamma_f^0 + \sum_f \boldsymbol{T}_f^n \Gamma_f^0 + \sum_f (\boldsymbol{T}'_f)^* \Gamma_f^0, & \end{aligned} \tag{32}$$

$$\boldsymbol{v}_P^{n+1} = \frac{\boldsymbol{u}_P^{n+1} - 4\boldsymbol{u}_P^n + \boldsymbol{u}_P^{n-1}}{2\Delta t} = \frac{\delta \boldsymbol{u}_P^{n+1} - 3\boldsymbol{u}_P^n + \boldsymbol{u}_P^{n-1}}{2\Delta t}. \tag{33}$$

- composite scheme [25]: a simplified version is implemented here, where the Crank-Nicolson and backward schemes are applied alternately.

In the above expressions, the velocity is introduced as an auxiliary variable, defined as the temporal derivative of the displacement, $v = \frac{\partial \boldsymbol{u}}{\partial t}$. The velocity at the current time step is subsequently expressed in terms of the displacement and its increment by employing the same temporal discretisation scheme.

The fully discretised momentum equation can now be written in the form of a linear algebraic equation, which for a cell P takes the form:

$$\begin{aligned}\mathbf{A}_P^{\delta u}\cdot\delta\boldsymbol{u}_P^{n+1}+\sum_N\mathbf{A}_N^{\delta u}\cdot\delta\boldsymbol{u}_N^{n+1}+\\ \mathbf{A}_P^{\delta u,\delta p}\cdot\delta p_P^{n+1}+\sum_N\mathbf{A}_N^{\delta u,\delta p}\cdot\delta p_N^{n+1}=\mathbf{r}_P^{\delta u},\end{aligned}\tag{34}$$

where $\mathbf{A}_P^{\delta u}$ and $\mathbf{A}_N^{\delta u}$ denote the central (diagonal) and neighbour (off-diagonal) tensorial coefficients associated with the displacement increment field, while $\mathbf{A}_P^{\delta u,\delta p}$ and $\mathbf{A}_N^{\delta u,\delta p}$ denote the corresponding vectorial coefficients associated with the pressure increment field. The source vector $\mathbf{r}_P^{\delta u}$ on the right-hand side depends on the solution due to the explicit treatment of certain terms (e.g., traction, non-orthogonal, and skewness corrections). The central and neighbour coefficients in Equation (34) as well as the right-hand side vector are defined in Appendix B for the first-order implicit Euler scheme.

3.2.2. Discretised Pressure Equation

The discretised momentum equation represented by Equation (34) must be complemented by an additional system of algebraic equations for the unknown cell-centre pressure increment field. In this study, the collocated (cell-centred) finite volume method is applied to numerically solve incompressible fluid flow, where the discretised pressure equation is derived by combining the discretised momentum and continuity equations using the Rhie–Chow momentum interpolation procedure [8].

For cell P, the discrete form of the incompressibility condition (21) reads:

$$\sum_f\boldsymbol{n}_f^{1+1/2}\cdot\delta\boldsymbol{u}_f^{n+1}\,\Gamma_f^{1+1/2}=0,\tag{35}$$

where the integration is performed on the cell faces mapped to the configuration at $t=t^{n+1/2}$, which represents the intermediate state between the previous and current configurations and will hereafter be denoted by an m subscript or superscript, that is, $t^m=t^{n+1/2}$. This approach yields the highest accuracy, as shown in [4]. Taking into account the above-introduced convention, the simplified representation of the discrete form of the incompressibility condition now reads as follows:

$$\sum_f\boldsymbol{n}_f^{m}\cdot\delta\boldsymbol{u}_f^{n+1}\,\Gamma_f^{m}=0.\tag{36}$$

The cell-face volume increment $\delta\Omega_f^{n+1}=\boldsymbol{n}_f^m\cdot\delta\boldsymbol{u}_f^{n+1}\,\Gamma_f^m$ in Equation (36) is calculated using the Rhie–Chow interpolation procedure [8] as follows:

$$\begin{aligned}\delta\Omega_f^{n+1}=&\boldsymbol{n}_f^m\cdot\overline{\overline{(\delta\boldsymbol{u})}}_f^{m,n+1}\,\Gamma_f^m+\delta\Omega_f^{\mathrm{CRC}}-\\ &-\left[\overline{\left(\frac{A_P^{\delta u}}{\Omega_P^0}\right)_f}^{m}\right]^{-1}\left[\widehat{\boldsymbol{d}}_f^m\cdot(\nabla_m\delta p)_f^{n+1}-\widehat{\boldsymbol{d}}_f^m\cdot\overline{(\nabla_m\delta p)_f^*}^{m}\right]\Gamma_f^m,\end{aligned}\tag{37}$$

where the interpolated cell-face displacement increment $\overline{\overline{(\delta\boldsymbol{u})}}_f^{m,n+1}$ is corrected by a term proportional to the difference between the pressure increment derivative interpolated to the face and the derivative computed directly at the face. This correction acts as a low-pass filter, preventing pressure-displacement decoupling and suppressing oscillations in the pressure increment field. The diagonal coefficient $A_P^{\delta u}$ is a scalar quantity and consists of only contributions from the temporal and normal derivative term in the discretised momen-

tum equation [first two terms at the right-hand side of Equation (A1)] (The contribution arising from the normal derivative of the normal displacement increment is neglected, as it is tensorial in nature and would significantly increase the complexity of deriving the pressure increment equation.). Following the block-coupled solution procedure proposed for incompressible fluid flow in [9], only the interpolated gradient of the pressure increment term is treated explicitly after discretisation, while the remaining two terms are implicit. The cell-face derivative of pressure increment $\widehat{\boldsymbol{d}}_f^m \cdot (\nabla_m \delta p)_f^{n+1}$ in Equation (37) is discretised using the central differencing formula:

$$\widehat{\boldsymbol{d}}_f^m \cdot (\nabla_m \delta p)_f^{n+1} = \frac{\delta p_N^{n+1} - \delta p_P^{n+1}}{|\boldsymbol{d}_f^m|}, \tag{38}$$

where $\widehat{\boldsymbol{d}}_f^m = \boldsymbol{d}_f^m / |\boldsymbol{d}_f^m|$ is the unit vector along the line $\overline{PN}$ (see Figure 1). Here, it should be noted that the pressure derivative is taken along the line connecting two neighbouring cell centers instead of along the cell-face normal direction. According to [14], this simplification does not violate the efficiency of the low-pass filter.

Rhie–Chow momentum-weighted interpolation is widely used to prevent pressure–velocity decoupling in simulations of incompressible flow on meshes with a collocated variable arrangement. The original Rhie–Chow interpolation [8] was proposed for steady-state fluid flow simulations, and its direct application to transient problems can result in temporally inconsistent behaviour. Various modifications to the original formulation have been proposed for transient problems (see, for example, ref. [26] and the comprehensive review in [14]). Here, we propose a temporally consistent Rhie–Chow interpolation that can be applied to transient simulations of incompressible solid deformation described by the governing equations in the pressure-displacement formulation. The modification is implemented through an explicit correction term $\delta\Omega_f^{\mathrm{CRC}}$ in Equation (37), which is provided for first-order accurate implicit Euler temporal discretisation schemes in Appendix C.

Using Equation (37), the discretised incompressibility condition (35) can be transformed into a discretised pressure increment equation, which can be expressed as a linear algebraic equation for the pressure increment of any cell P:

$$\begin{aligned} A_P^{\delta p} \cdot \delta p_P^{n+1} + \sum_N A_N^{\delta p} \cdot \delta p_N^{n+1} + \\ \mathbf{A}_P^{\delta p, \delta \boldsymbol{u}} \cdot \delta \boldsymbol{u}_P^{n+1} + \sum_N \mathbf{A}_N^{\delta p, \delta \boldsymbol{u}} \cdot \delta \boldsymbol{u}_N^{n+1} = r_P^{\delta p}, \end{aligned} \tag{39}$$

where $A_P^{\delta p}$ and $A_N^{\delta p}$ are diagonal and off-diagonal scalar coefficients related to the unknown pressure increment field, $\mathbf{A}_P^{\delta p, \delta \boldsymbol{u}}$ and $\mathbf{A}_N^{\delta p, \delta \boldsymbol{u}}$ are diagonal and off-diagonal vectorial coefficients related to the unknown displacement increment field, and $r_P^{\delta p}$ is the right-hand side of the linear equation. The central and neighbour coefficients in Equation (39) as well as the right-hand side term are defined in Appendix B.

As will be shown later, Equations (34) and (39) are used to assemble a block linear system, which is solved for cell-centre displacement increment $\delta \boldsymbol{u}_P$ and cell-centre pressure increment δp_P. After cell-centre unknowns are obtained, Rhie–Chow interpolation Formula (37) is used to calculate cell-face volume increment (volume sweep by the cell-faces), which is then used to calculate "conservative" cell-face displacement increment as follows:

$$\delta \boldsymbol{u}_f^{n+1} = [\boldsymbol{I} - (\boldsymbol{n}\boldsymbol{n})_f^m] \cdot \overline{\overline{(\delta \boldsymbol{u}_P)}}_f^{m,n+1} + \frac{\delta \Omega_f^{n+1}}{\Gamma_f^m} \boldsymbol{n}_f^m. \tag{40}$$

In this way, the calculated displacement increment is guaranteed to satisfy the discrete incompressibility condition (35).

As can be seen, the pressure increment equation is discretised on the computational mesh in the intermediate configuration, which is half a time step behind the current (deformed) configuration. This implies that the computational mesh may become highly distorted in cases of large deformations, which can in turn slow the convergence of the solution procedure due to the increasing contribution of the explicit skewness correction in the first term on the right-hand side of Equation (37). The accuracy of the pressure-increment and displacement-increment gradient calculations may also be reduced on a distorted mesh.

3.2.3. Calculation of Gradients

A very important component of the solution procedure is the calculation of the gradients of unknown fields. Pressure increment gradient is required at cell-centres, while displacement increment gradient has to be calculated at the cell-centres as well as at the cell-face centres. The cell-centre gradient of all fields is calculated using the least-squares linear fit [27]. This method produces a second-order-accurate gradient regardless of local mesh quality.

The face-centre gradient of displacement increment is used to evaluate the explicit part at the right-hand side of Equation (22). The full cell-centre gradient is composed of the normal and tangential components as follows:

$$(\nabla_0 \delta \boldsymbol{u})_f = (\boldsymbol{n}^0 \boldsymbol{n}^0 \cdot \nabla_0 \delta \boldsymbol{u})_f + (\nabla_{0t} \delta \boldsymbol{u})_f, \tag{41}$$

where the normal derivative of displacement increment $(\boldsymbol{n}^0 \cdot \nabla_0 \delta \boldsymbol{u})_f$ is calculated using Equation (25), while the tangential face-centre gradient is calculated by taking the tangential component of the interpolated cell-centre gradient:

$$(\nabla_{0t} \delta \boldsymbol{u})_f = (\boldsymbol{I} - \boldsymbol{n}_f^0 \boldsymbol{n}_f^0) \cdot {}^0\overline{(\nabla_0 \delta \boldsymbol{u})}_f, \tag{42}$$

where $\boldsymbol{n}_f^0$ is the cell-face unit normal vector. The tangential gradient at the boundary cell face is evaluated by second-order accurate linear extrapolation of the neighbouring cell-centre gradients.

3.2.4. Mesh Vertices Displacement

Before discretising the pressure-increment equation, the mesh is moved to an intermediate configuration by updating the vertices' positions from their reference locations to the intermediate ones. The corresponding vertex displacements are reconstructed from the cell-centre displacements of the surrounding cells using a weighted least-squares method with a linear fitting function (see details in [23]).

3.2.5. Initial and Boundary Conditions

To start the transient simulation, it is necessary to specify the displacement and velocity at the initial time for all cell centres in the computational mesh. Boundary conditions must be applied to the cell faces that lie on the domain boundary.

Up to this point, the discretisation procedure has been described only for internal cell faces. To discretise the governing equations at the boundary cell faces, it is necessary to account for the specified boundary conditions. This is explained below for two typical boundary conditions: specified displacement increment (Dirichlet boundary condition) and specified traction (Neumann boundary condition).

If a specified displacement increment boundary condition is used, the normal derivative of the displacement increment in Equation (23) is approximated using the scheme defined by Equation (25), where $\delta \boldsymbol{u}_N$ is replaced by the specified boundary cell-face displacement increment $\delta \boldsymbol{u}_b$. At the same boundary, a zero normal-derivative boundary condition is applied for the pressure increment field, so that Equation (37) yields a boundary-face volume increment corresponding to the specified displacement increment. The zero normal-derivative boundary condition is also used to update the pressure increment at the corresponding boundary cell-face at the end of each outer iteration of the iterative solution procedure.

For boundary faces where specified traction increment boundary condition is applied, the traction increment term $\delta \boldsymbol{T}_f$ in Equation (22) is added to the source term (right-hand side), and the traction correction term $\delta \boldsymbol{T}'_f$ is set to zero. At the same boundary faces, the specified pressure increment boundary conditions are applied, where the pressure increment value is calculated from the constitutive equation using the gradient of the displacement increment at the boundary from the previous iteration. The cell-face displacement increment term in Equation (37) is defined implicitly at the boundary cell-face b as follows:

$$\overline{\overline{(\delta \boldsymbol{u})}}^{m}_{b}{}^{n+1} = \delta \boldsymbol{u}_P^{n+1} + \left(\frac{\partial \delta \boldsymbol{u}}{\partial n} \right)^{*}_{b} \delta^{m}_{bn}, \tag{43}$$

where $\delta \boldsymbol{u}_P^{n+1}$ is the displacement increment at the centre of the cell next to the considered boundary face b, δ^{m}_{bn} is the normal distance between the boundary face centre b and the adjacent cell-centre P, the normal derivative of the displacement increment is defined as follows:

$$\left(\frac{\partial \delta \boldsymbol{u}}{\partial n} \right)^{*}_{b} = \frac{\delta \boldsymbol{u}^{*}_{b} - \delta \boldsymbol{u}^{*}_{P}}{\delta^{m}_{bn}}. \tag{44}$$

The superscript $*$ denotes quantities obtained in the previous iteration, and the boundary face displacement increment $\delta \boldsymbol{u}^{*}_{b}$ is defined by Equation (40). In this equation, the tangential component of the displacement increment (first term on the right-hand side) is computed to satisfy the constitutive relation at traction-specified boundary faces.

3.2.6. Final Block-Coupled System of Linear Algebraic Equations

By combining the discretised momentum Equation (34) with the discretised pressure-increment (incompressibility condition) Equation (39), one obtains the following coupled system of algebraic equations for each cell P in the computational mesh:

$$\mathbf{A}_P \cdot \mathbf{\Phi}_P + \sum_N \mathbf{A}_N \cdot \mathbf{\Phi}_N = \mathbf{R}_P, \tag{45}$$

where $\mathbf{A}_P$ and $\mathbf{A}_N$ are the 4×4 dense matrices representing the diagonal and off-diagonal coefficients of the coupled linear system, obtained by combining the corresponding coefficients of the discretised momentum Equation 34) and the discretised pressure Equation (39), as is illustrated for the diagonal coefficient $\mathbf{A}_P$ in Figure 2. For each cell P, the 4×1 vector $\mathbf{\Phi}$ is defined, which consists of the cell-centre unknown fields: the three components of the cell-centre displacement increment vector and the cell-centre pressure increment. For example, for cell P this vector of unknowns is given by the following: $\mathbf{\Phi}_P = [(\delta \boldsymbol{u}_P)_x \ (\delta \boldsymbol{u}_P)_y \ (\delta \boldsymbol{u}_P)_z \ \delta p_P]^{\mathrm{T}}$. The 4×1 vector $\mathbf{R}_P$ on the right-hand side of Equation (45) is composed of the corresponding right-hand side vectors of the linear systems (34) and (39), as follows: $\mathbf{R}_P = [(\mathbf{r}_P^{\delta \boldsymbol{u}})^x \ (\mathbf{r}_P^{\delta \boldsymbol{u}})^y \ (\mathbf{r}_P^{\delta \boldsymbol{u}})^z \ r_P^{\delta p}]^{\mathrm{T}}$. After composing the

system of linear algebraic equations (45) for all cells in the computational mesh, the corresponding global linear system is obtained:

$$\mathbf{A} \cdot \mathbf{\Phi} = \mathbf{R}, \tag{46}$$

where $\mathbf{A}$ is the square block matrix, $\mathbf{\Phi}$ is the block vector of unknown fields and $\mathbf{R}$ is the block vector of the right-hand side, and their dimension is equal to the number of cells in the computational mesh. The block linear system (46) is solved using the Block–Jacobi preconditioner and the BiSGSTAB solver.

$$\mathbf{A}_P = \begin{bmatrix} \begin{bmatrix} (\mathbf{A}_P^{\delta \boldsymbol{u}})_{xx} & (\mathbf{A}_P^{\delta \boldsymbol{u}})_{xy} & (\mathbf{A}_P^{\delta \boldsymbol{u}})_{xz} \\ (\mathbf{A}_P^{\delta \boldsymbol{u}})_{yx} & (\mathbf{A}_P^{\delta \boldsymbol{u}})_{yy} & (\mathbf{A}_P^{\delta \boldsymbol{u}})_{yz} \\ (\mathbf{A}_P^{\delta \boldsymbol{u}})_{zx} & (\mathbf{A}_P^{\delta \boldsymbol{u}})_{zy} & (\mathbf{A}_P^{\delta \boldsymbol{u}})_{zz} \end{bmatrix} & \begin{bmatrix} (\mathbf{A}_P^{\delta \boldsymbol{u}, \delta p})_x \\ (\mathbf{A}_P^{\delta \boldsymbol{u}, \delta p})_y \\ (\mathbf{A}_P^{\delta \boldsymbol{u}, \delta p})_z \end{bmatrix} \\ \begin{bmatrix} (\mathbf{A}_P^{\delta p, \delta \boldsymbol{u}})_x & (\mathbf{A}_P^{\delta p, \delta \boldsymbol{u}})_y & (\mathbf{A}_P^{\delta p, \delta \boldsymbol{u}})_z \end{bmatrix} & \begin{bmatrix} (\mathbf{A}_P^{\delta p}) \end{bmatrix} \end{bmatrix}$$

Figure 2. Diagonal 4×4 matrix coefficient $\mathbf{A}_P$ of the block matrix at the node P, consisting of corresponding diagonal coefficients of the discretised linear momentum and pressure increment equations. Green color signifies diagonal tensorial coefficients associated with the displacement increment field. Blue and yellow colors denote the corresponding vectorial coefficients associated with the pressure increment field. Red color denotes diagonal scalar coefficients related to the unknown pressure increment field.

3.3. Solution Procedure

The overall solution procedure is summarised in Algorithm 1 and can be categorized as the fixed-point/Picard iteration method. The main part of the solution procedure is the outer iteration loop that starts with the assembly of the global linear system (46), where the elements of the vector $\mathbf{R}$ in the current iteration (k) are calculated using the values of unknown fields obtained in the previous outer iteration ($k-1$). The outer iteration loop repeats while the norm of the residual of the system (46) remains greater than the predefined convergence tolerance, i.e., $|\mathbf{A}^{k-1} \cdot \mathbf{\Phi}^{k-1} - \mathbf{R}^{k-1}| > \epsilon$.

Algorithm 1 Block-coupled solution procedure.

while $t^{n+1} < t_{\text{end}}$ **do**
  Initialize fields: $\delta p_{\text{P}}^{n+1}$ and $\delta \boldsymbol{u}_{\text{P}}^{n+1}$
  $k = 0$
  while $|\mathbf{A}^{k-1} \cdot \mathbf{\Phi}^{k-1} - \mathbf{R}^{k-1}| > \epsilon$ **do**
    $k = k + 1$
    Calculate cell displacement increment gradient $(\nabla \delta \boldsymbol{u})_P^{n+1}$
    Calculate face displacement increment gradient $(\nabla \delta \boldsymbol{u})_f^{n+1}$
    Update total displacement gradients and corresponding deformation gradients
    Update $\boldsymbol{\sigma}_P = \boldsymbol{\sigma}(\boldsymbol{F}_P^{k-1}, p_P^{k-1})$ and $\boldsymbol{\sigma}_f = \boldsymbol{\sigma}(\boldsymbol{F}_f^{k-1}, p_f^{k-1})$ using $\cdots$
    $\cdots$ selected constitutive equation
    Assemble linear system (34)
    Move mesh to "intermediate" configuration
    Assemble linear system (39)
    Assemble global linear system $\mathbf{A}^{k-1} \cdot \mathbf{\Phi}^{k} = \mathbf{R}^{k-1}$ and solve it for $\delta \boldsymbol{u}_P^{n+1}$ and δp_P^{n+1}
    Calculate cell-face sweep volume using Rhie–Chow interpolation (37)
    Calculate conservative cell-face displacement increment $\delta \boldsymbol{u}_f^{n+1}$ using Equation (39)
    Move mesh to initial configuration
    Update total displacement and total pressure:
      $\boldsymbol{u}_P^{n+1} = \boldsymbol{u}_P^{n} + \delta \boldsymbol{u}_P^{n+1}$
      $\boldsymbol{u}_f^{n+1} = \boldsymbol{u}_f^{n} + \delta \boldsymbol{u}_f^{n+1}$
      $p_P^{n+1} = p_P^{n} + \delta p_P^{n+1}$
  end while
  Calculate cell-centre velocity $\boldsymbol{v}_P$ using selected temporal scheme
  $t^{n+1} = t^{n} + \Delta t$
end while

4. Results

In this section, seven test cases are presented to demonstrate the solver's performance across different deformation regimes. The infinite plate with a circular hole is first used to assess accuracy in the linear elastic regime. Next, uniaxial stretch and simple shear tests highlight the nonlinear capabilities of the solver under elementary deformation modes. Inflation of a pressurised cylinder illustrates both steady-state and transient behaviour, including a temporal accuracy analysis of the Euler, backward, trapezoidal, and composite discretisation schemes. The heart tissue beam test evaluates the solver's accuracy and stability in transient problems involving large rotations and displacements. Solver performance with the HGO constitutive model is demonstrated by inflating a rat carotid artery. Finally, ventricle inflation serves as a realistic three-dimensional benchmark. In all cases, results obtained with the FV method are compared with analytical or FE solutions obtained using FEBio software version 2.7.0 suit [28,29].

4.1. Infinite Plate with a Circular Hole Subjected to Uniform Tension

A plate with a circular hole in its centre is loaded with uniform tension in the axial direction (see Figure 3). The problem is considered as the plane strain. If the radius of the hole is small compared to the dimensions of the plate, then the analytical solution obtained for an infinitely large plate describes the stress and displacement distribution around the hole [30]:

$$\sigma_{xx}(r,\theta) = t_x\left[1 - \frac{a^2}{r^2}\left(\frac{3}{2}\cos 2\theta + \cos 4\theta\right) + \frac{3}{2}\frac{a^4}{r^4}\cos 4\theta\right],$$
$$\sigma_{yy}(r,\theta) = t_x\left[-\frac{a^2}{r^2}\left(\frac{1}{2}\cos 2\theta - \cos 4\theta\right) - \frac{3}{2}\frac{a^4}{r^4}\cos 4\theta\right],$$
$$\sigma_{xy}(r,\theta) = t_x\left[-\frac{a^2}{r^2}\left(\frac{1}{2}\sin 2\theta + \sin 4\theta\right) + \frac{3}{2}\frac{a^4}{r^4}\sin 4\theta\right],$$

$$u_x(r,\theta) = \frac{at_x}{8\mu}\left\{\frac{r}{a}(k+1)\cos\theta + 2\frac{a}{r}[(k+1)\cos\theta + \cos 3\theta] - 2\frac{a^3}{r^3}\cos 3\theta\right\},$$
$$u_y(r,\theta) = \frac{at_x}{8\mu}\left\{\frac{r}{a}(k-3)\sin\theta + 2\frac{a}{r}[(1-k)\sin\theta + \sin 3\theta] - 2\frac{a^3}{r^3}\sin 3\theta\right\},$$

where r and θ are polar coordinates, a is the hole radius, μ is the shear modulus, and $k = 3 - 4\nu$ is the Kolosov constant for plane strain deformation.

The plate material is assumed to be linear elastic, isotropic, and incompressible (Poisson's ratio $\nu = 0.5$), with Young's modulus $E = 10^9$ Pa. Owing to the problem's symmetry, only a quarter of the plate is modelled, as shown in Figure 4 (shaded area). Following earlier studies of the same problem, e.g., [19], the exact solution corresponding to $t_x = 10$ kPa is prescribed on all traction-specified boundaries (top and right dashed edges) to eliminate finite-domain effects.

Spatial accuracy is demonstrated by comparing results obtained using the proposed FV solver with the corresponding analytical solution. This comparison was first conducted for three meshes of similar resolution, each consisting of a different cell shape: quadrilateral, triangular, and polygonal (In reality, the mesh is 3-D and consists of one layer of prismatic cells with quadrilateral, triangular, and polygonal base.), as shown in Figure 4. Figure 5 presents a comparison of the x-component of the displacement vector and the xx-component of the stress tensor with analytical results along the AB boundary of the plate. Similarly, Figure 6 shows a comparison of the y-component of the displacement vector and the yy-component of the stress tensor along the DE boundary. Very good agreement

is observed between the analytical solution and the FV solver results for all three cell shapes. Among the mesh types tested, the polygonal mesh required the fewest outer iterations to achieve convergence (53 iterations), followed by the hexagonal mesh (98 iterations) and the tetrahedral mesh (138 iterations). The convergence tolerance was set to $\epsilon = 10^{-9}$.

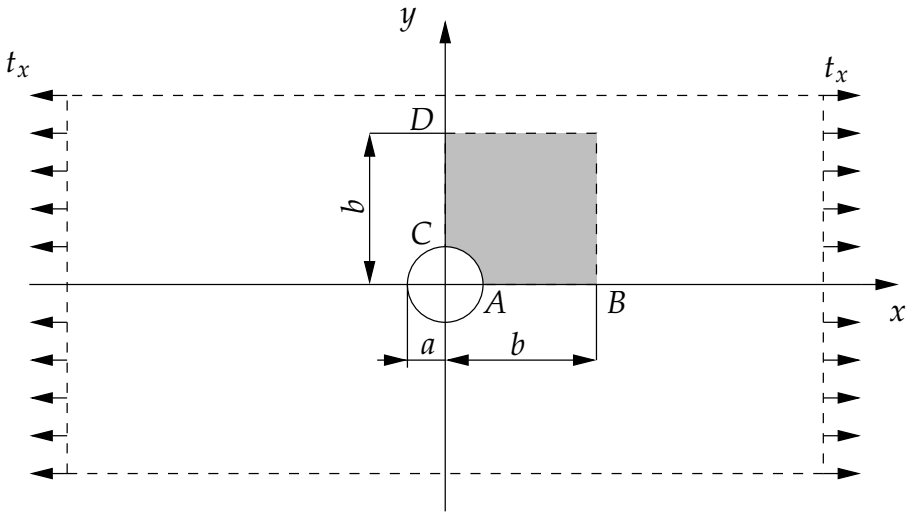

Figure 3. Geometry of the spatial computational domain for the flat plate with a circular hole ($a = 0.5$ m, $b = 2$ m, $E = 1 \times 10^7$ Pa, $\nu = 0.5$, $t_x = 10{,}000$ Pa) [23]. Arrows indicate the applied pressure stretching the plate. Only the grey region is included in the simulations.

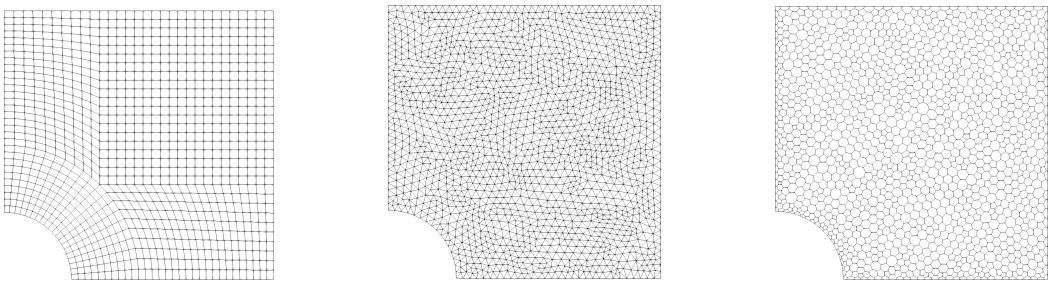

(**a**) Quadrilateral cells (**b**) Triangular cells (**c**) Polygonal cells

Figure 4. Plate with a circular hole discretised using three cell types at comparable resolution: quadrilateral cells, triangular cells, and polygonal cells. (**a**) Quadrilateral cells (**b**) Triangular cells (**c**) Polygonal cells.

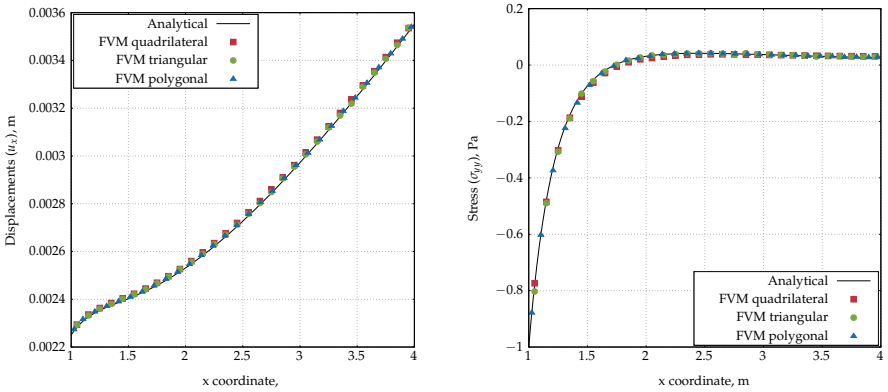

(**a**) x-component of the displacement (**b**) yy-component of the Cauchy stress along the AB boundary

Figure 5. Plate with a circular hole. Comparison of the (**a**) x-component of the displacement and the (**b**) yy-component of the Cauchy stress along the AB boundary of the spatial domain (see Figure 3).

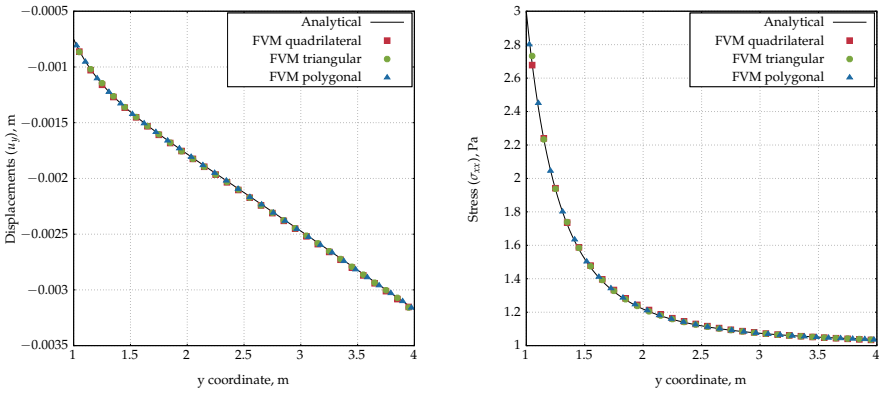

(**a**) y-component of the displacement (**b**) xx-component of the Cauchy stress

Figure 6. Plate with a circular hole. Comparison of the (**a**) y-component of the displacement and the (**b**) xx-component of the Cauchy stress along the DE boundary of the spatial domain (see Figure 3).

The order of spatial accuracy of the proposed FV solver is evaluated by performing simulations on four quadrilateral meshes with successively increasing numbers of cells (1000, 4000, 16,000, 64,000), with the coarsest mesh shown in Figure 4a. The cell-centre errors are calculated for displacement magnitude and xx-component of the Cauchy stress with respect to the available analytical solution, and the magnitude of the errors is computed using standard norms (L^1, L^2, and L^∞). Figure 7 presents the error norms as a function of the average cell size. Second-order accuracy is achieved for the displacement across all three norms, whereas for the xx-component of the Cauchy stress tensor, first-order accuracy is observed with respect to the L^∞ norm, while second-order accuracy is attained for the remaining two norms.

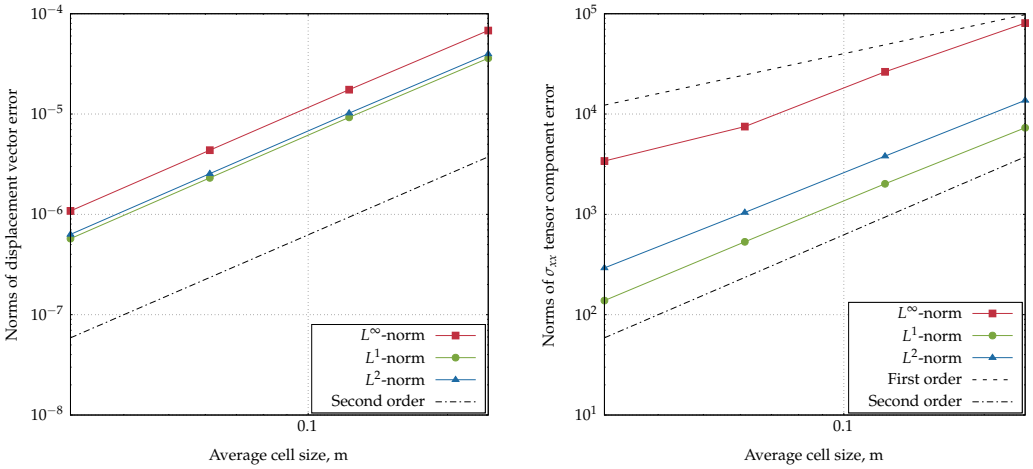

(**a**) Displacement magnitude error (**b**) Error of the xx-component of the Cauchy stress

Figure 7. Plate with a circular hole. (**a**) Displacement magnitude error and (**b**) Error of xx-component of the Cauchy stress, calculated with respect to the analytical solution and evaluated by the L^1, L^2, and L^∞ norms.

4.2. Uniaxial Extension and Simple Shear Tests

To test the solvers' nonlinear capabilities for fundamental types of deformation, uniaxial extension and simple shear tests are performed on a cube with dimensions 1 m × 1 m × 1 m. The cube is modeled as an incompressible material ($\nu = 0.5$). Both tests are solved using the Neo-Hookean and Guccione material laws. For the Neo-Hookean material, the shear modulus of the cube is $\mu = 10^6$ Pa. For the Guccione law, the material

properties are $C = 2 \times 10^6$ Pa, with $b_f = b_t = b_{fs} = 1$. A detailed description of the incompressible Guccione constitutive relation is provided in Appendix D.2. Although the application of the Neo-Hookean material law is not appropriate for these tests beyond the known maximum strain (i.e., 40% for uniaxial extension), the intention was to investigate how far the strain could be pushed using the proposed numerical model.

4.2.1. Uniaxial Extension Test

The simulation of uniaxial extension along the x-direction is performed on one quarter of the unit cube by applying symmetry boundary conditions on the xz- and xy-planes (see Figure 8). The yz-plane is also modeled as a symmetry plane to allow free contraction of the cube in the lateral directions. On the remaining boundaries, specified traction boundary conditions are applied, with the traction calculated from the available analytical solution. For uniaxial extension along the x-direction, the deformation gradient can be expressed in terms of the principal stretches as follows:

$$\boldsymbol{F} = \begin{bmatrix} \lambda_x & 0 & 0 \\ 0 & \lambda_y & 0 \\ 0 & 0 & \lambda_z \end{bmatrix}, \tag{47}$$

where $\lambda_y = \lambda_z = 1/\sqrt{\lambda_x}$ for the case of an incompressible material. For a given deformation gradient, the Cauchy stress and the corresponding traction on the cube boundaries are calculated based on the selected constitutive relation. Simulations are performed for the principal stretch λ_x varying in the range 1–1.8.

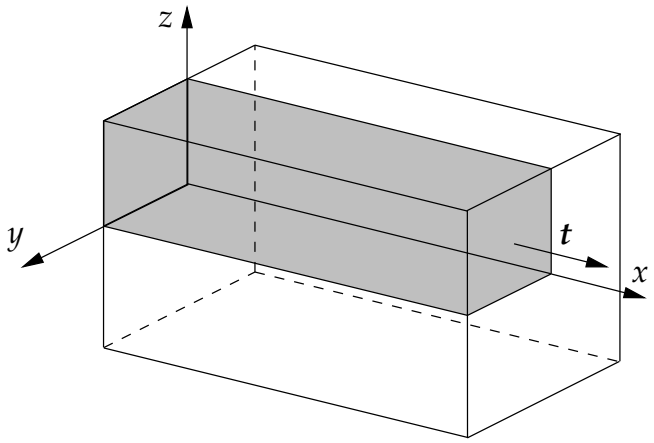

Figure 8. Uniaxial extension of a block. Spatial domain in reference configuration and boundary conditions. Arrow signifies applied traction on the boundary. Only the grey region is included in the simulations.

Figure 9 shows the deformed configuration of the cube for $\lambda_x = 1.8$, calculated using the incompressible Neo-Hookean material. For the same material, Figure 10 presents a comparison between the numerical and analytical solutions for the stretches $\lambda_y = \lambda_z$, the hydrostatic pressure, and the xx-component of the Cauchy stress. The numerical results closely follow the analytical solution. An analogous comparison for the incompressible Guccione material is shown in Figure 11.

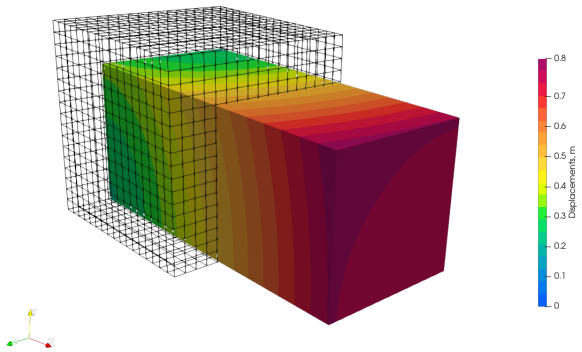

Figure 9. Uniaxial extension of a block: reference configuration (black outline) and displacement field on the deformed configuration for $\lambda_x = 1.8$.

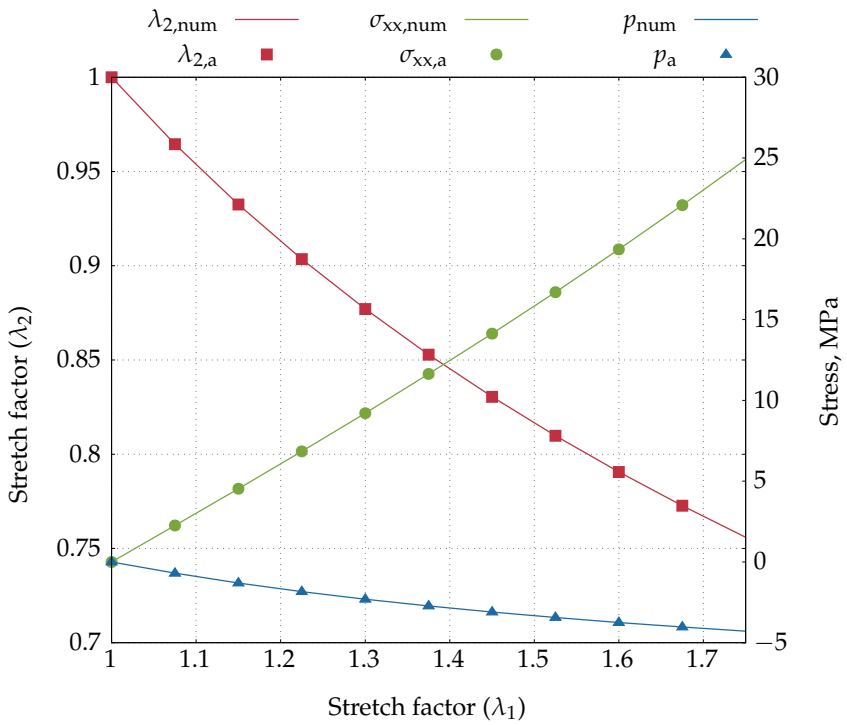

Figure 10. Uniaxial extension of a block: analytical vs numerical results for the incompressible Neo-Hookean material. Plots of λ_2, σ_{xx}, and pressure p as functions of λ_1.

4.2.2. Simple Shear Test

The simple shear test involves a deformation in which parallel planes of the material slide past each other. The deformation gradient for simple shear in the xy-plane is defined as follows:

$$\boldsymbol{F} = \begin{bmatrix} 1 & \gamma & 0 \\ 0 & 1 & 0 \\ 0 & 0 & 1 \end{bmatrix}, \tag{48}$$

where γ is the shear strain. In this study, a simple shear deformation is applied to the unit cube shown in Figure 12. A zero-displacement boundary condition is imposed on the bottom surface, while fixed traction boundary conditions are applied on the remaining surfaces, with the traction calculated using the selected constitutive relation (Neo-Hookean or Guccione) and the deformation gradient defined in Equation (48). The shear strain is varied in the range 0–0.6.

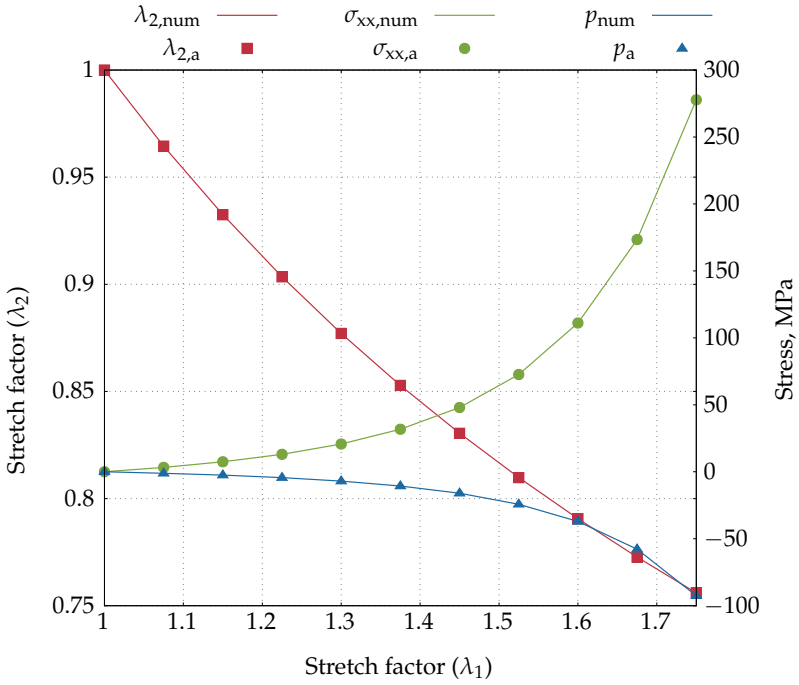

Figure 11. Uniaxial extension of a block: analytical vs numerical results for the incompressible Guccione material. Plots of λ_2, σ_{xx}, and pressure p as functions of λ_1.

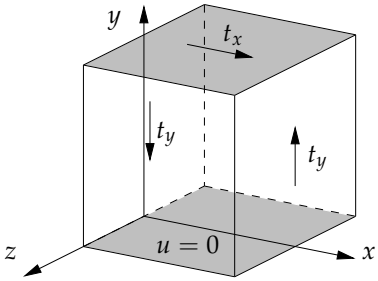

Figure 12. Simple shear test of a unit cube: reference configuration and boundary conditions.

The reference and final (deformed) configurations of the cube are shown in Figure 13 for the Neo-Hookean material model and for $\gamma = 0.6$. The current configuration is coloured by the displacement field, where one can note parallel and horizontal contour lines, as is expected for the case considered. Figure 14 presents a comparison between the exact and numerically calculated displacement of the top surface of the cube for the Neo-Hookean and Guccione material models as a function of the specified shear strain γ, where the exact value of the displacement for the unit cube is $u_{x,a} = \gamma \times 1$ m.

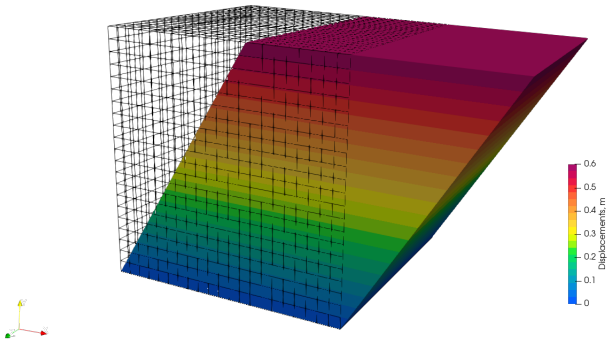

Figure 13. Simple shear test: Current and reference configuration of the cube for shear strain $\gamma = 0.6$ obtained with the Neo-Hookean material model.

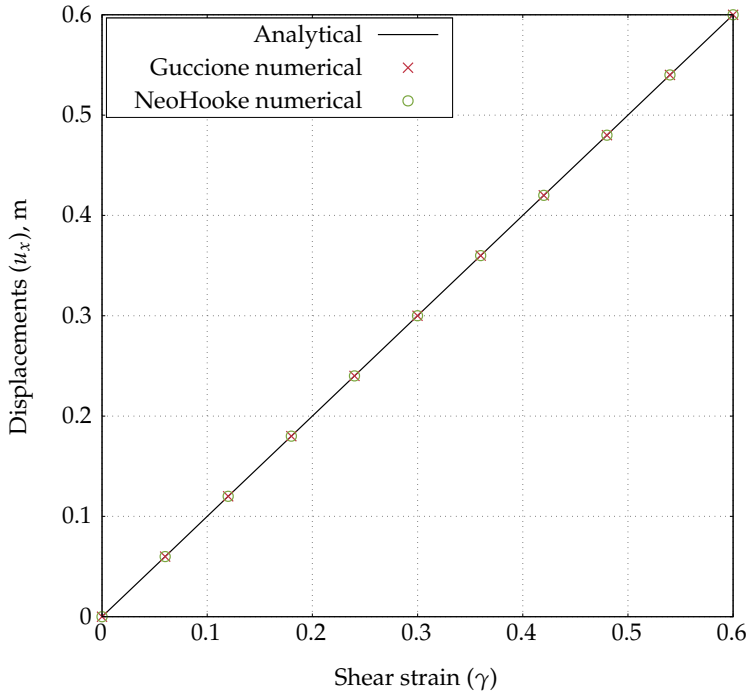

Figure 14. Simple shear test: comparison of numerically computed top-surface displacement with the exact solution as a function of shear strain γ, for Neo-Hookean and Guccione material laws.

4.3. Inflation of a Thick-Wall Cylinder

An infinitely long, thick-walled cylinder with inner radius $r_i = 8$ m and outer radius $r_o = 16$ m, is subjected to pressure $p = 10$ MPa. This case was also solved in [5]. A plane strain deformation is assumed. The material of the cylinder is assumed to be incompressible ($\nu = 0.5$) and hyperelastic with Young's modulus $E = 1000$ MPa. The behaviour of the incompressible hyperelastic material is described by the Neo-Hookean constitutive relation.

Exploiting the geometric and loading symmetry, only one quarter of the domain is modeled, as shown in Figure 15, with symmetry boundary conditions applied on the corresponding planes. The outer wall is modeled as traction-free. The analytical solution for this problem is provided in Appendix E.

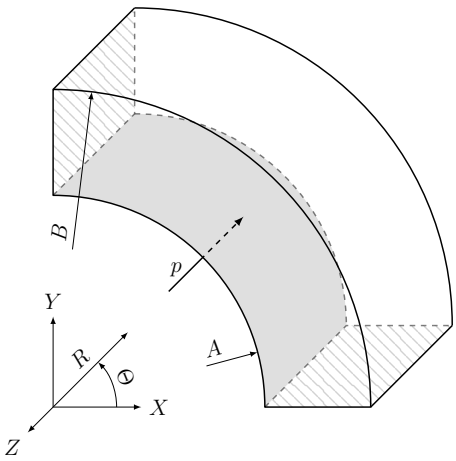

Figure 15. Inflation of a pressurised cylinder: 1/4-section in reference configuration.

Figure 16 shows a hexahedral mesh with 65 cells and a polyhedral mesh with 1338 cells. These meshes, together with two finer hexahedral meshes consisting of 260 and 1040 cells, were used to compute the solution for an internal pressure of $p = 100$ MPa. The predicted

radial displacement, radial stress, hoop stress, and pressure along the radius are compared to the analytical solution in Figure 17. The solutions obtained on the hexahedral meshes converge consistently to the analytical solution with increasing mesh resolution, and good agreement is also observed for the solution obtained on the polyhedral mesh. The temporal accuracy analysis, presented in the continuation, is performed on the results obtained with the finer hexahedral mesh.

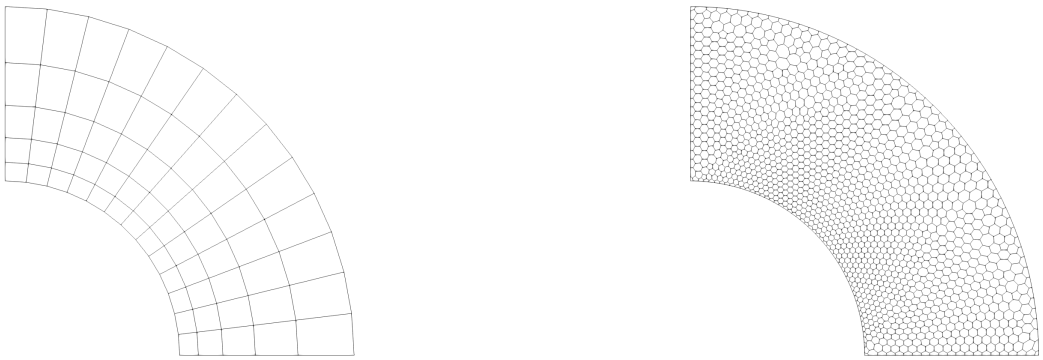

(**a**) (**b**)

Figure 16. Inflation of a pressurised cylinder: coarsest hexahedral mesh with 65 cells (**a**) and polyhedral mesh with 1338 cells (**b**) used in the test case.

To assess temporal accuracy, the case was solved using different time-step sizes: 10^{-2} s, 5×10^{-3} s, 2.5×10^{-3} s, 1.25×10^{-3} s, 6.25×10^{-4} s and 10^{-5} s. The prescribed pressure at the inner surface is increased linearly from $p = 0$ MPa to $p = 100$ MPa over a time period 0.01 s. The accuracy analysis is carried out at the time instance $t = 0.01$ s. The cell-centre displacement error is computed for the solution obtained with the five largest time-step sizes with respect to the reference solution obtained with the smallest time-step size 10^{-5} s. The magnitude of the cell-centre displacement error was quantified using the L^{∞} norm.

The temporal accuracy is assessed for both linear and non-linear deformation regimes employing four temporal discretisation schemes: Euler, backward, Crank–Nicolson, and composite. The corresponding displacement error norms are presented in Figure 18 as functions of the time-step size. For both deformation regimes, the Euler scheme exhibits the expected first-order convergence of the error, whereas the remaining schemes attain the expected second-order convergence.

The average number of outer iterations per time-step was 52 for both the Euler and backward temporal discretisation schemes used with a time-step size of 10^{-2} s. The number of outer iterations gradually increases as the time-step size decreases. In all runs, the convergence tolerance was set to $\epsilon = 10^{-10}$.

Finally, the long-term temporal response of the cylinder was analysed for the case in which the internal pressure was first increased linearly from $p = 0$ MPa to $p = 100$ MPa over the interval $t = 0$ s to $t = 0.01$ s, and then decreased linearly back to $p = 0$ MPa over the interval $t = 0.01$ s to $t = 0.02$ s. For this scenario, the total energy of the isolated system must remain constant for $t > 0.02$ s, in the absence of external forcing. Figure 19 shows the temporal response of kinetic, potential, and total energy obtained using a backward temporal discretisation scheme, where the total energy is computed as a sum of kinetic and potential energy, and potential energy is calculated according to the Neo-Hookean constitutive relation. One can note the expected behaviour of the total energy at the time instance $t = 0.02$ s. Other second-order temporal discretisation schemes show similar behaviour.

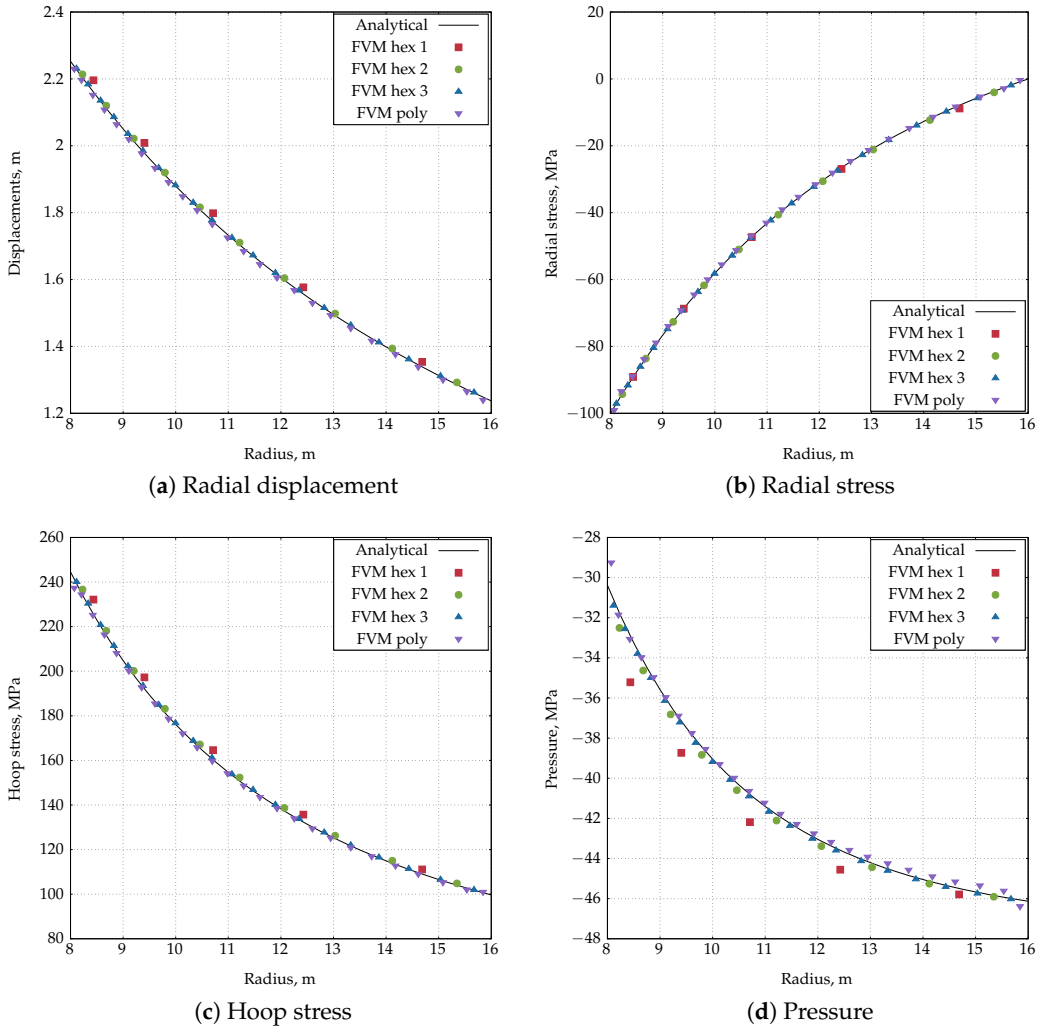

(**a**) Radial displacement (**b**) Radial stress

(**c**) Hoop stress (**d**) Pressure

Figure 17. Inflation of a pressurised cylinder: predicted results for three hexahedral meshes and one polyhedral mesh compared to the analytical solution. (**a**) Radial displacement; (**b**) Radial stress; (**c**) Hoop stress; (**d**) Pressure.

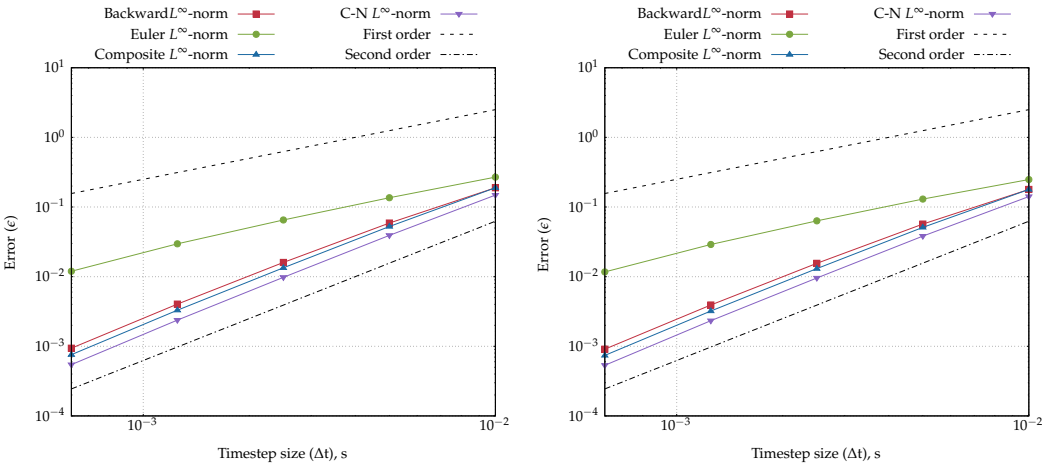

(**a**) The non-linear solver (**b**) The linear solver

Figure 18. Inflation of a pressurised cylinder: temporal accuracy study for Euler, backward Euler, composite, and Crank–Nicolson schemes using both linear and non-linear solver. (**a**) The non-linear solver; (**b**) The linear solver.

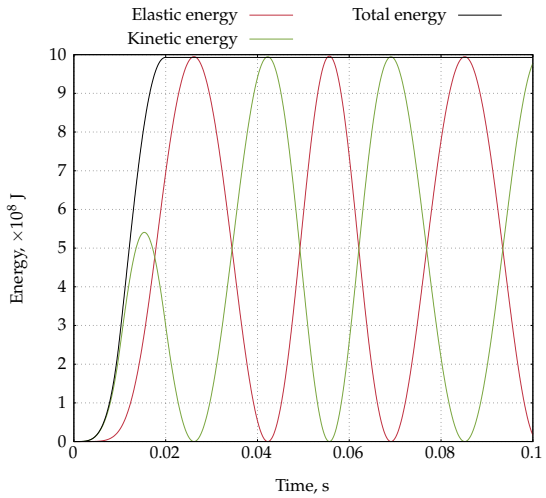

Figure 19. Inflation of a pressurised cylinder: temporal evolution of the kinetic, elastic, and total energy of the system for the long-term response obtained using the backward temporal discretisation scheme.

4.4. Heart Tissue Beam

In this benchmark test case proposed by Land et al. [31], one considers deformation of a thick beam of 10 mm length, and $(1\text{ mm} \times 1\text{ mm})$ quadratic cross section (see Figure 20). This example represents a simplified strip of cardiac tissue, commonly used to study the fundamental mechanical behaviour of myocardium under bending. The beam test assesses the solver's accuracy and stability in transient problems involving large rotations and displacements, while avoiding geometric complexity and enabling direct comparison with published benchmark solutions. The test case is analysed for two hyperelastic constitutive models: incompressible Guccione model as originally proposed in [31] (fibre direction along long axis, constitutive parameters: $C = 2000$ Pa, $b_f = 8$, $b_t = 2$, $b_{fs} = 4$) and incompressible Neo-Hookean model with shear modulus $\mu = 15{,}000$ Pa. The properties of the incompressible Guccione model approximately correspond to the heart tissue properties.

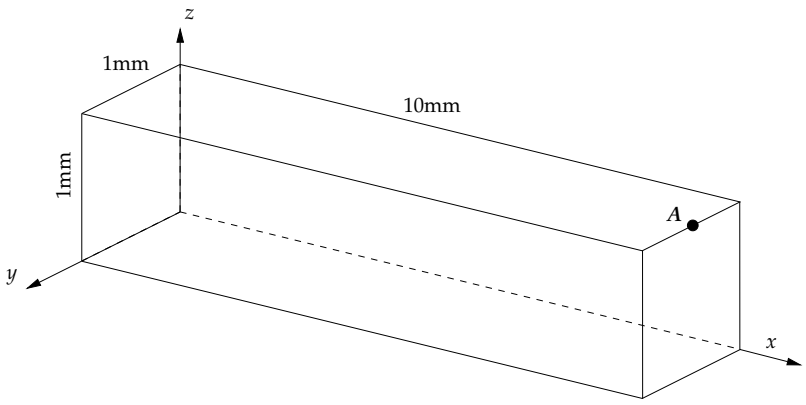

Figure 20. Heart tissue beam: reference configuration, with point A indicated.

In the first step, a mesh sensitivity study is performed where a steady-state FV solution is compared with the corresponding solution obtained using FEBio software suite [28,29], verified on selected test cases proposed in [31]. The beam is discretised by a uniform structured mesh, and it is subjected to a uniform pressure load of 4 Pa on the bottom side, while the left side is fixed in all directions. Figure 21 shows the z-coordinate of the tip point A (defined in Figure 20) as a function of cell dimension, where one can note consistent convergence toward the FE benchmark solution. Figure 22 shows the maximal deflection of the beam. Results are given for a $50 \times 5 \times 5$ computational mesh.

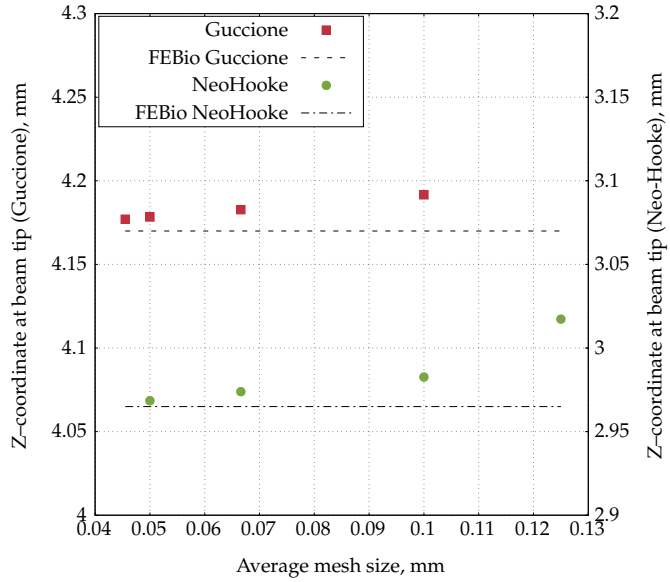

Figure 21. Heart tissue beam: Beam tip point z-coordinate for different mesh densities for Neo-Hookean material law. Results converge to a consensus solution as the number of volumes increases.

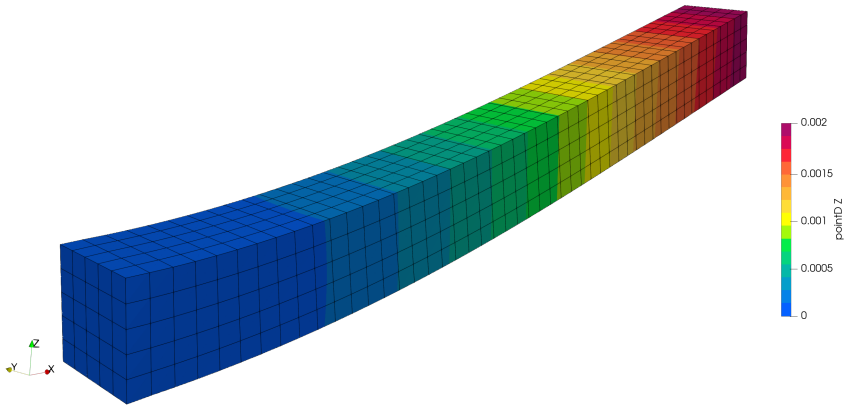

Figure 22. Heart tissue beam: the computational mesh ($50 \times 5 \times 5$) in deformed configuration. Colors represent z-component of the displacement vector obtained for the Neo-Hookean material law.

A temporal accuracy study was performed with the Neo-Hookean model, following the procedure outlined in Section 4.3. The results confirm first- and second-order accuracy for the Euler and backward time discretisation schemes, respectively, as illustrated in Figure 23, for both linear and nonlinear models. Results obtained with the trapezoidal scheme are not reported because numerical instabilities were observed at the smallest time-step sizes. To address this issue in nonlinear cases, the composite scheme proposed by Bathe and Noh [25] was employed. For sufficiently small time-step sizes, the composite scheme proposed by Bathe and Noh [25] attains second-order accuracy for both linear and nonlinear model.

To examine the solver's stability over the long-term temporal response of the beam, an unsteady simulation is performed to capture the beam's oscillatory response induced by a short-term pressure impulse applied to its bottom surface. The pressure is linearly increased to a maximum value of 4 Pa by 0.02 s and then decreased back to 0 Pa by 0.04 s. Simulations are conducted using the Euler, backward, composite, and trapezoidal temporal schemes with a time-step size of $\Delta t = 10^{-4}$ s, and run until $t = 1$ s. Figures 24–27 show the displacement and velocity of the beam tip, along with the kinetic, elastic, and total energy of the system as functions of time, calculated using the Euler, backward, composite, and trapezoidal temporal schemes. The backward, trapezoidal, and composite schemes

exhibit a stable long-term response, with constant amplitudes of displacement, velocity, kinetic, and elastic energy. The total energy of the system remains constant over time once the external loading is removed. As expected, the Euler scheme shows damping of the amplitudes.

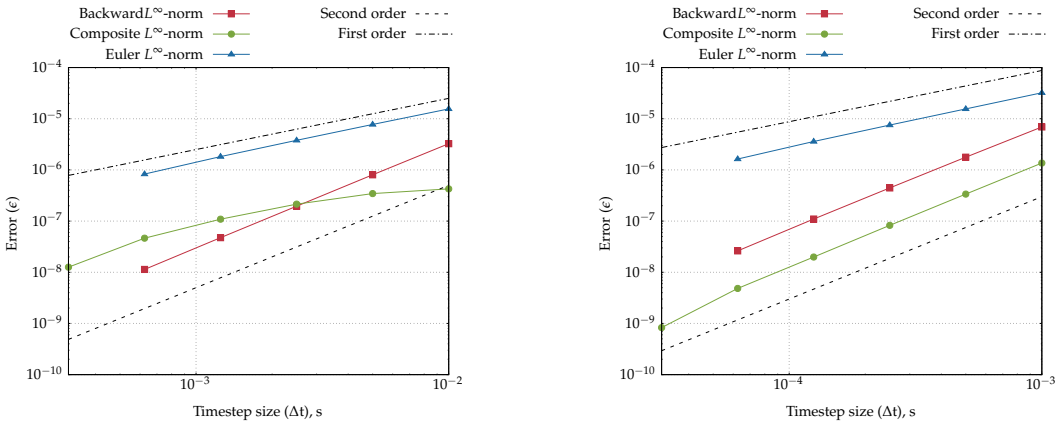

(**a**) The non-linear solver (**b**) The linear solver

Figure 23. Heart tissue beam: Time convergence study of the displacements for Euler and backward temporal schemes for both linear and non-linear solver. (**a**) The non-linear solver; (**b**) The linear solver.

4.5. Inflation of a Rat Carotid Artery

This test case is based on the experimental study reported in [32], where carotid arteries were harvested from rats and subjected to internal pressurisation, during which the outer radius was measured as a function of the applied pressure. The test case isolates key physiological mechanisms—pressure-driven deformation, non-linear and anisotropic soft-tissue behaviour, and collagen fibre recruitment—while avoiding anatomical complexity. The availability of experimental pressure–radius data and well-established FE benchmark results makes this case particularly suitable for quantitative model validation. Based on these experimental data, the HGO material model [15] was calibrated in [33]. This constitutive model effectively captures the anisotropic mechanical response of arterial walls by decomposing the strain energy density function into two components: an isotropic part, dominant at low pressures and consistent with a Neo-Hookean material behaviour, and an anisotropic part, which becomes prominent at higher pressures, which models the effect of progressive straightening of helically oriented collagen fibres. The material parameters were defined as follows [33]: Young's modulus $E = 132.69$ kPa, $k_1 = 206$ Pa, and $k_2 = 1.465$. The collagen fibers were assumed to be symmetrically oriented at $\pm 39.76^\circ$ with respect to the circumferential direction.

In this study, numerical simulations of the rat carotid artery inflation, as described above, are performed following a similar FE study by Sun et al. [34]. The computational domain is defined as a cylindrical segment with an inner radius of $r_i = 3$ mm, an outer radius of $r_o = 4$ mm, and a length of 5 mm. Axial displacements are constrained. Owing to geometric and loading symmetry, only one quarter of the domain is modelled, as illustrated in Figure 28, with appropriate symmetry boundary conditions applied on the corresponding planes. The outer wall is assumed to be traction-free, while an internal pressure of $p = 25$ kPa is applied to the inner wall through 100 loading steps.

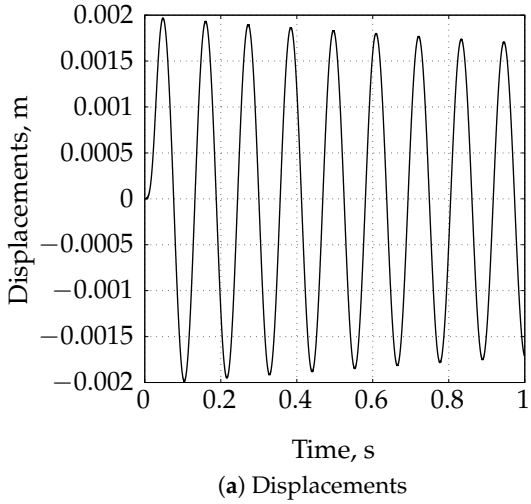

(**a**) Displacements

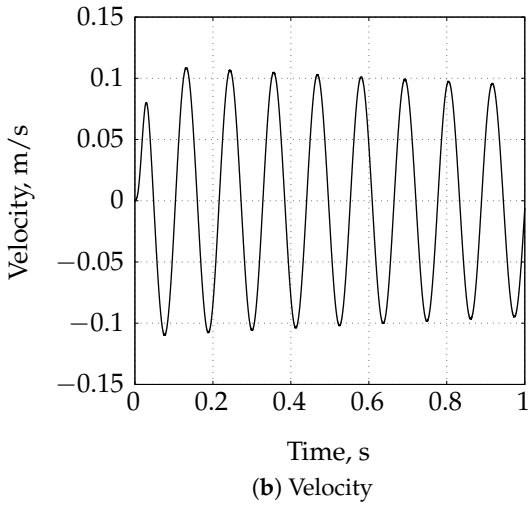

(**b**) Velocity

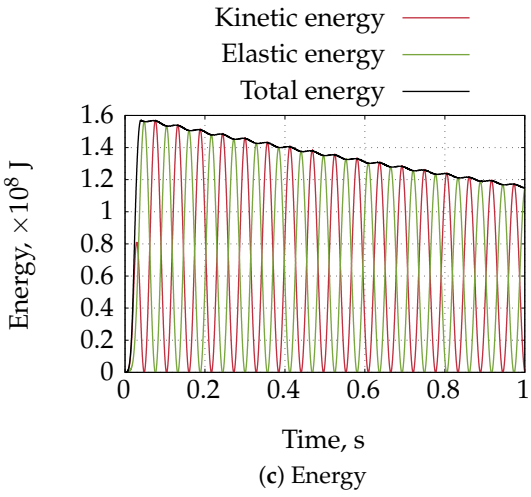

(**c**) Energy

Figure 24. Heart tissue beam: Displacement and velocity of the beam tip and energy of the system as functions of time, calculated using the Euler temporal discretisation scheme. (**a**) Displacements; (**b**) Velocity; (**c**) Energy.

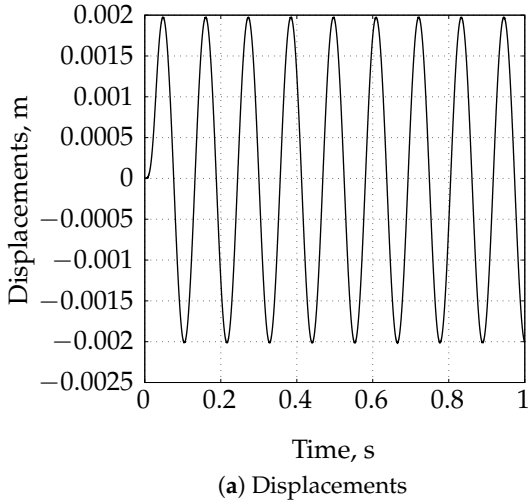

(**a**) Displacements

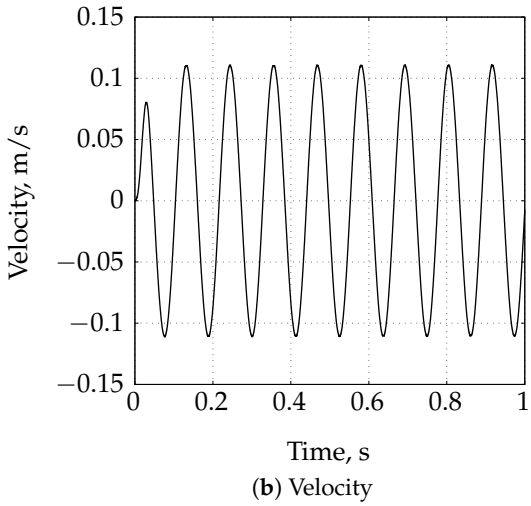

(**b**) Velocity

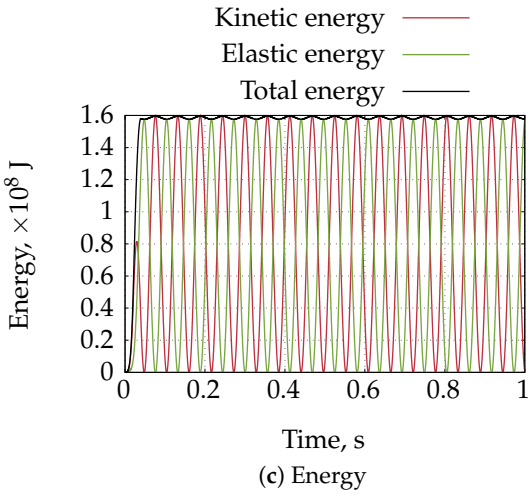

(**c**) Energy

Figure 25. Heart tissue beam: Displacement and velocity of the beam tip and energy of the system as functions of time, calculated using the backward temporal discretisation scheme. (**a**) Displacements; (**b**) Velocity; (**c**) Energy.

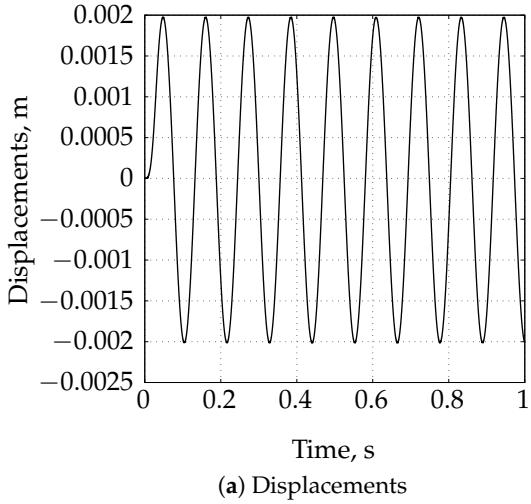

(**a**) Displacements

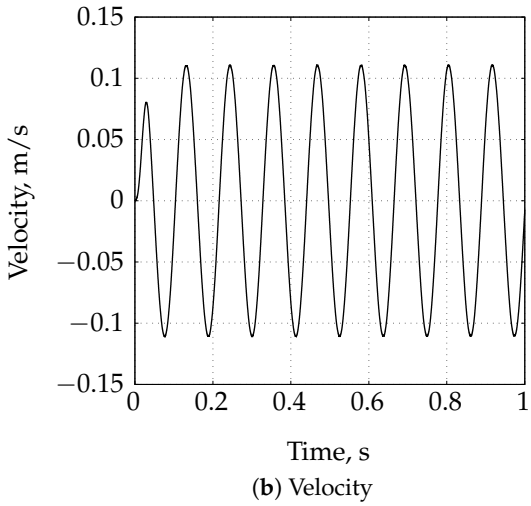

(**b**) Velocity

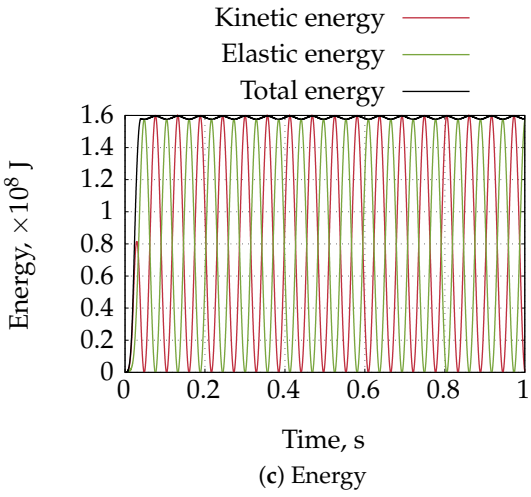

(**c**) Energy

Figure 26. Heart tissue beam: Displacement and velocity of the beam tip and energy of the system as functions of time, calculated using the composite temporal discretisation scheme. (**a**) Displacements; (**b**) Velocity; (**c**) Energy.

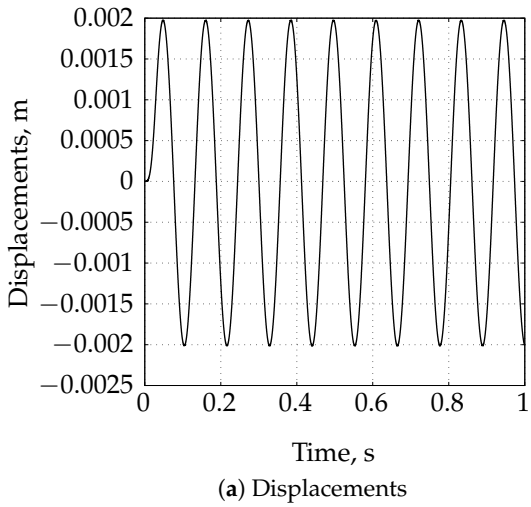

(**a**) Displacements

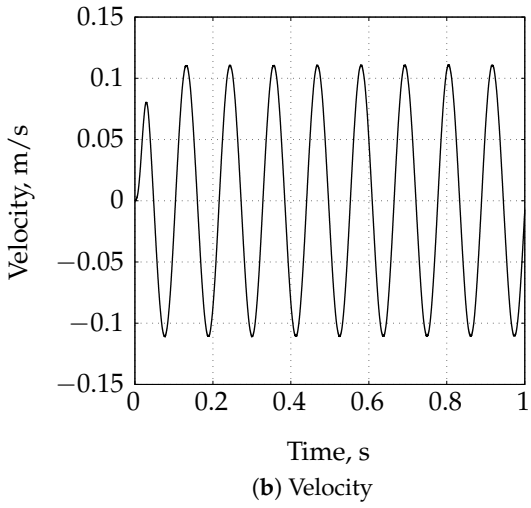

(**b**) Velocity

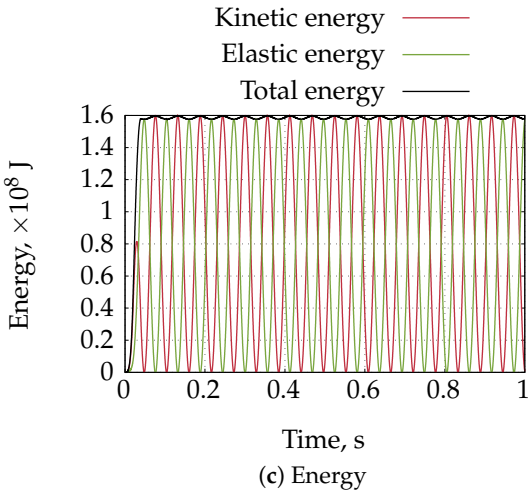

(**c**) Energy

Figure 27. Heart tissue beam: Displacement and velocity of the beam tip and energy of the system as functions of time, calculated using the trapezoidal temporal discretisation scheme. (**a**) Displacements; (**b**) Velocity; (**c**) Energy.

Figure 28 also shows the deformed geometry at the final loading step. The evolution of the inner and outer radii of the cylindrical surfaces as a function of the applied inner pressure, obtained with the FV solver, is presented in Figure 29. Results for the inner surface are compared with experimental data from [32] and FE results from [34], while results

for the outer surface are compared against FE results only. Overall, good agreement is observed. On average, 445 outer iterations per loading step were required for a convergence tolerance of $\epsilon = 10^{-7}$.

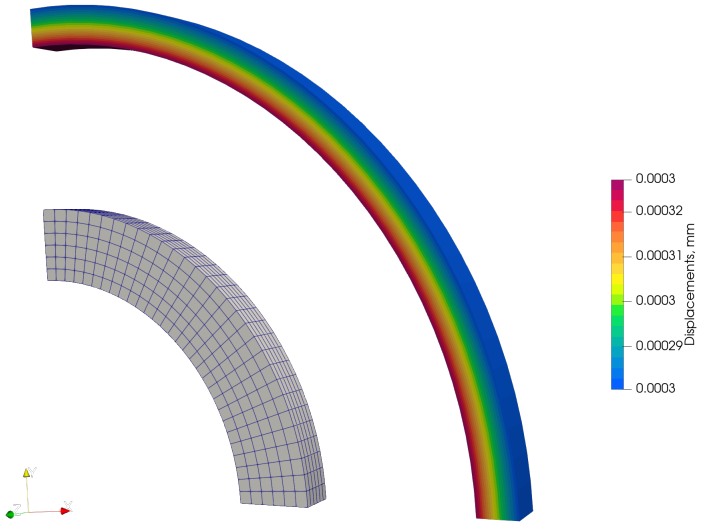

Figure 28. Inflation of a rat carotid artery: reference configuration with mesh (one-quarter cylindrical domain) and deformed configuration at the final loading step, coloured by the displacement field.

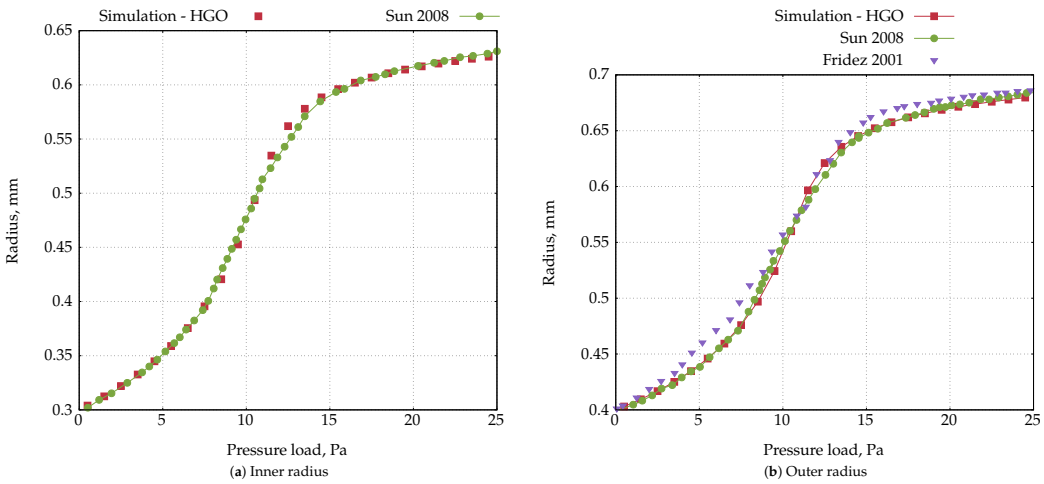

(**a**) Inner radius (**b**) Outer radius

Figure 29. Inflation of a rat carotid artery: the variation of the inner radius with respect to internal pressure (**a**), and the corresponding variation of outer radius (**b**).

4.6. Inflation of an Idealised Ventricle

Inflation of an idealised ventricle (Figure 30) was proposed by Land et al. [31] as a benchmark problem for cardiac mechanics software. The case is three-dimensional and static, with finite hyperelastic deformation. The initial geometry is defined as a truncated ellipsoid:

$$x = r_s \sin(u)\cos(v), \quad y = r_s \sin(u)\sin(v), \quad z = r_l \cos(u). \tag{49}$$

The endocardial (inner) surface is defined as $r_s = 7$ mm, $r_l = 17$ mm, $u \in \left[-\pi, -\arccos\frac{5}{17}\right]$, and $v \in [-\pi, \pi]$. The epicardial (outer) surface is defined as $r_s = 10$ mm, $r_l = 20$ mm, $u \in \left[-\pi, -\arccos\frac{5}{20}\right]$, and $v \in [-\pi, \pi]$. The implicitly defined base plane is positioned at $z = 5$ mm. The behaviour of hyperelastic material is described by the transversely isotropic incompressible Guccione model [16], where the parameters are $C = 10$ kPa, $b_f = b_t = b_{fs} = 1$ (the specified parameters produce isotropic behaviour). The geometry

of the idealised ventricle is axisymmetric, but a three-dimensional model is constructed, which should yield an axisymmetric solution.

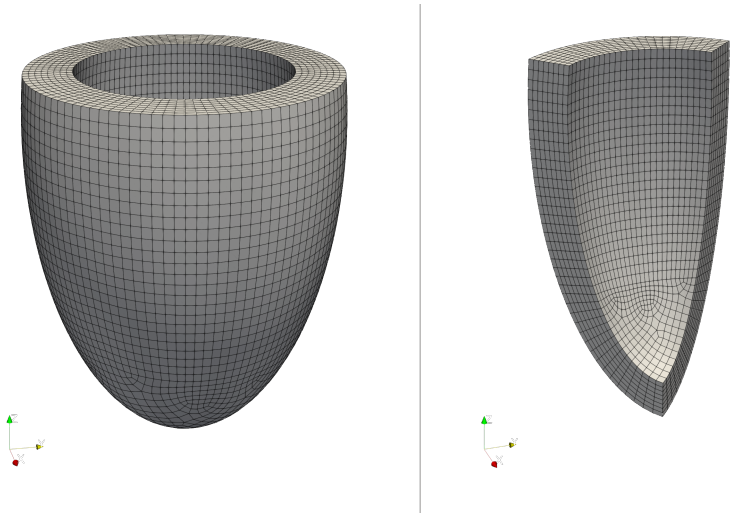

Figure 30. Inflation of an idealized ventricle in the reference configuration. The entire domain is shown on the left; the computational domain (one quarter of the whole domain) is shown on the right.

One quarter of the axi-symmetric domain is considered, as shown in Figure 30. The geometry is discretised entirely with hexahedral prisms. The epicardial surface is modelled as traction-free, while a fixed displacement boundary condition is prescribed on the top base plane. Symmetry boundary conditions are applied to the two cutting planes used to extract the quarter section of the ventricle. The endocardial surface is subjected to an internal pressure of 2300 Pa. The internal pressure value of 10,000 Pa proposed in [31] could not be reached with the proposed FV solver due to the occurrence of unphysical pressure oscillations.

The load is applied incrementally in steps of 100 Pa. Simulations are performed on three successively refined meshes containing 2728, 16,992, and 38,292 cells. The corresponding average numbers of outer iterations per loading step were 139, 134, and 141 for a convergence tolerance of $\epsilon = 10^{-7}$. The reference solution is obtained using the FEBio software on the finest mesh. Figure 31 shows the magnitude of the apex displacement at the endocardial and epicardial surfaces as a function of the pressure load applied to the endocardial surface. The solution obtained using the proposed FV solver consistently converges with mesh refinement toward the reference FE solution. Figure 32 shows a comparison of the ventricle shape at a loading pressure of 2300 Pa. Figure 32a shows the ventricle wall midline in its undeformed and deformed configurations obtained using FV and FEBio solvers. Similarly, Figure 32b shows the undeformed and deformed configuration for a line on the endocardial surface. In both cases, one can observe very good agreement between FV and FE results.

The simulations described above (performed using the incompressible Guccione constitutive model) were repeated with the incompressible Neo-Hookean constitutive model, with the shear modulus set to $\mu = 4000$ kPa, corresponding to the initial shear modulus of the Guccione model. The maximum achievable pressure load on the endocardial surface was 1700 Pa for both the proposed FV solver and the FE solver. The remaining boundary conditions were identical to those described previously. The average number of outer iterations per loading step was 56, 63, and 82 for the coarse, medium, and fine meshes, respectively, with the same convergence tolerance as above.

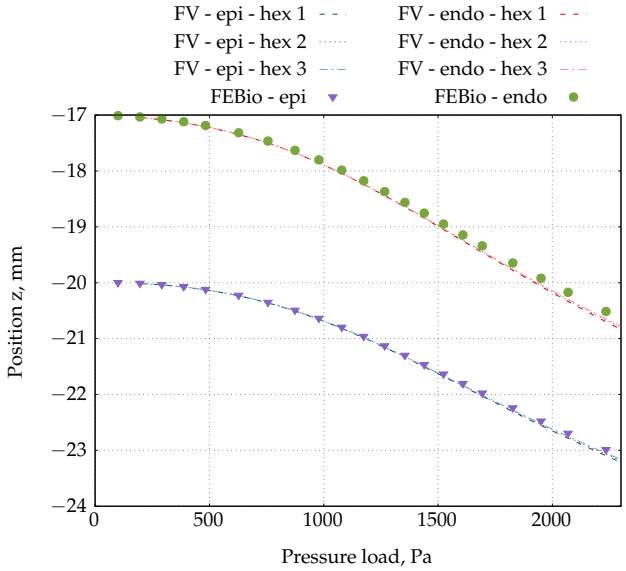

Figure 31. Ventricle inflation: comparison of the apex displacement at the endocardial and epicardial surfaces during ventricular inflation, obtained using FV and FE simulations.

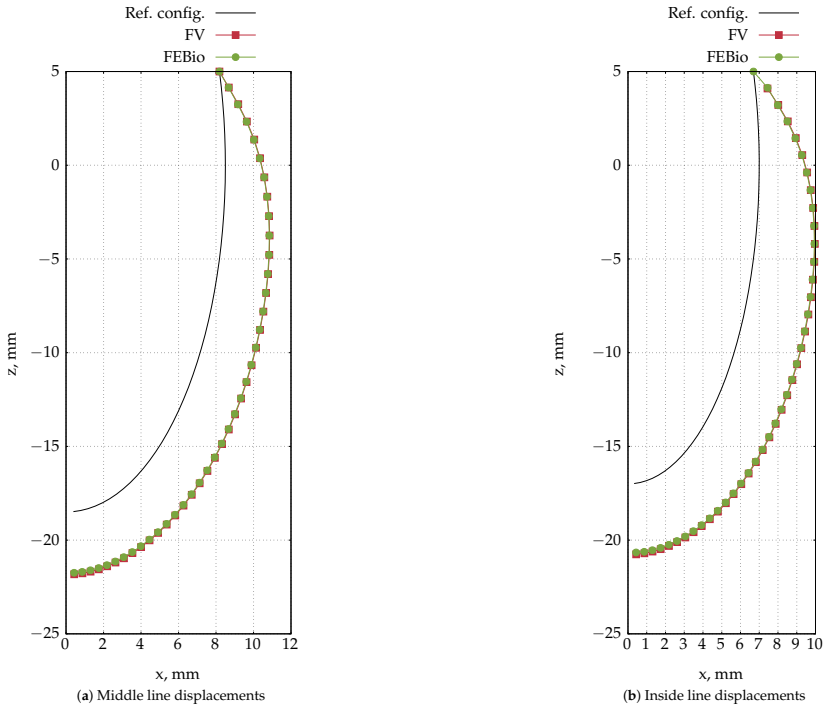

Figure 32. Inflation of an idealised ventricle: deformed configuration of the ventricle wall midline and inside line obtained using FV and FE solvers for loading pressure 2300 Pa. (**a**) Middle line displacements; (**b**) Inside line displacements.

Figure 33 illustrates the apex displacement magnitude at the endocardial and epicardial surfaces as a function of the applied internal pressure load, showing convergence toward the reference results with mesh refinement. Figure 34 compares the overall ventricle shape at an internal pressure of 1700 Pa, as computed with the proposed FV solver and the FEBio tool. Figure 34a presents the deformed configuration of the ventricle wall midline, while Figure 34b examines the deformed shape of a line on the endocardial surface. In both cases, the FV and FE results demonstrate very good agreement.

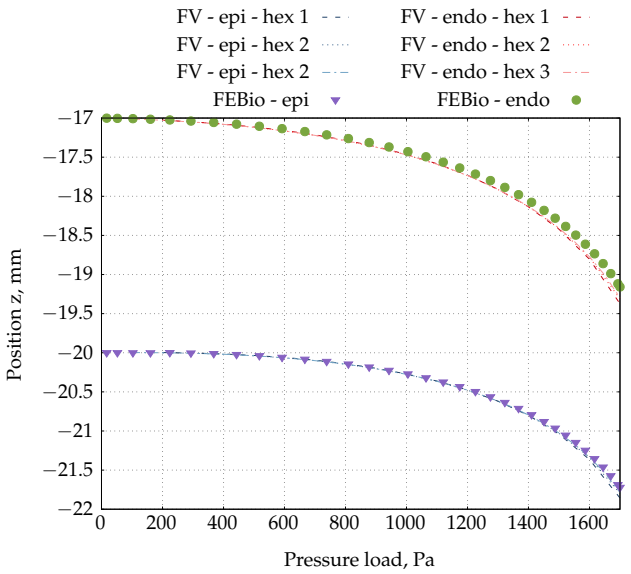

Figure 33. Inflation of an idealised ventricle: comparison of the apex displacement at the endocardial and epicardial surfaces during ventricular inflation, obtained using FV and FE simulations for Neo-Hookean material.

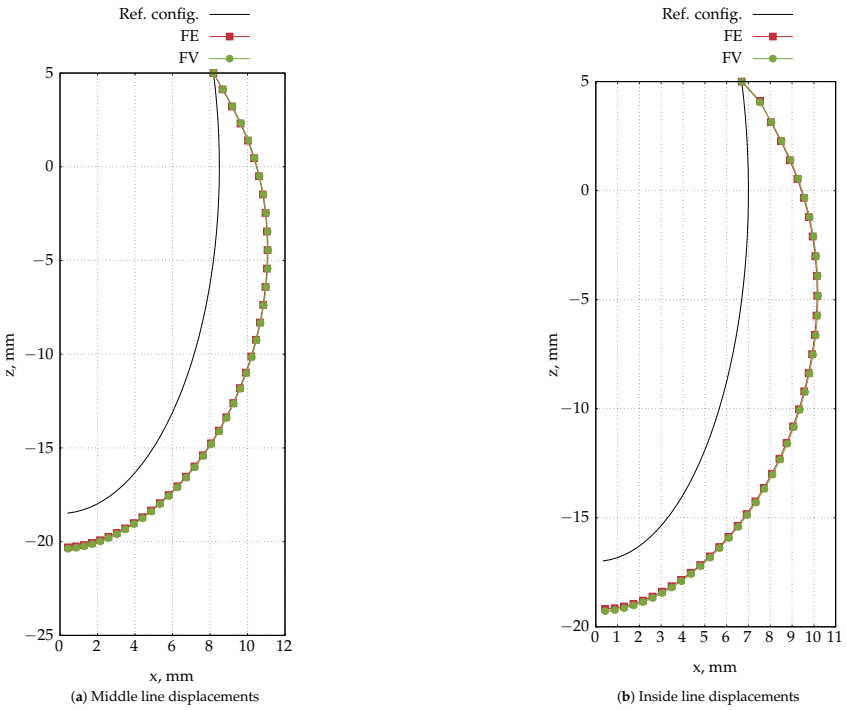

Figure 34. Inflation of an idealised ventricle: deformed configuration of the ventricle wall midline and inside line obtained using FV and FE solvers for loading pressure 2300 Pa with Neo-Hookean material. (**a**) Middle line displacements; (**b**) Inside line displacements.

5. Conclusions

This work presented a block-coupled second-order FV solver for incompressible elastic and hyperelastic solids, implemented within the solids4Foam toolbox for OpenFOAM. The solver was formulated using a pressure-displacement approach and can handle both linear elastic and nonlinear hyperelastic constitutive models relevant to vascular mechanics. Temporal accuracy was carefully addressed through the implementation of Euler, backward, Crank–Nicolson, and composite time integration schemes, each coupled with a temporally consistent Rhie–Chow interpolation.

A broad set of benchmark problems was used to verify and validate the solver, including small-strain linear elasticity, large-deformation cases, and physiologically motivated tests such as heart tissue beams, arterial inflation, and ventricular deformation. In all cases, the finite-volume (FV) results showed close agreement with analytical solutions or finite-element (FE) references, demonstrating second-order spatial accuracy under systematic mesh refinement. First- and second-order temporal accuracy was also verified, depending on the selected time-integration scheme. Importantly, the solver proved to be stable and robust for challenging transient problems while conserving energy under appropriate discretisation.

The solver's computational efficiency—measured by the number of outer iterations—is acceptable for the linear elastic and Neo-Hookean models, given that a fixed-point (Picard) iteration method was used for the nonlinear problems. The number of outer iterations is substantially larger for the Guccione and HGO models; this behaviour requires further investigation.

The presented method establishes a reliable and versatile FV framework for incompressible solid mechanics, providing a solid foundation for future developments in fluid–structure interaction simulations of vascular flows and cardiac mechanics. Ongoing work will focus on extending the solver toward fully coupled FSI applications, improving computational efficiency, and incorporating additional constitutive models to further broaden its applicability.

Author Contributions: Conceptualization, Ž.T.; methodology, Ž.T.; software, Ž.T.; validation, A.H. and P.M.; formal analysis, Ž.T. and A.H.; investigation, Ž.T.; resources, Ž.T.; data curation, Ž.T. and A.H.; writing—original draft preparation, Ž.T. and A.H.; writing—review and editing, Ž.T. and A.H.; visualization, A.H.; supervision, Ž.T.; project administration, Ž.T.; funding acquisition, Ž.T. and I.K. All authors have read and agreed to the published version of the manuscript.

Funding: This work was supported by grants from the Croatian Science Foundation (projects IP-2020-02-4016 and DOK-2021-02-3071, PI: Ž Tuković; projects IP-2018-01-3796 and DOK-2020-01-5698, PIs: D. Ozretić and I. Karšaj).

Data Availability Statement: The solver used for simulation described in this article will be made available by the authors on request.

Acknowledgments: The authors would like to thank the anonymous reviewers for their valuable comments and suggestions.

Conflicts of Interest: The authors declare no conflicts of interest.

Abbreviations

The following abbreviations are used in this manuscript:

FE	Finite Element
CSM	Computational Solid Mechanics
FV	Finite Volume
SIMPLE	Semi-Implicit Method for Pressure Linked Equations
FSI	Fluid–Structure Interaction
CV	Control Volume
HGO	Holzapfel–Gasser–Ogden
CRC	Consistent Rhie–Chow

Appendix A. Instantaneous Shear Modulus Approximation

The instantaneous (effective) shear modulus, μ_{eff}, is introduced in Equation (18) to account for the fact that the shear modulus generally changes during the deformation of a

hyperelastic body. In the case of the Neo-Hookean constitutive model, the instantaneous shear modulus is constant and equal to the standard shear modulus μ. For other hyperelastic constitutive relations, the instantaneous shear modulus is approximated using the procedure described below.

The approximated value of the instantaneous shear modulus is calculated by numerically performing a simple shear test in three mutually perpendicular planes at the cell centers, taking into account the current state of deformation. In this way, three different values of the shear modulus are obtained, and the maximum value is taken as the effective shear modulus.

The above-described procedure is performed at the end of every time step, and the obtained effective shear modulus is then used in the calculations of the following time step. It is important to note that the value of the effective shear modulus does not influence the final solution; it only affects the efficiency of the solution procedure (i.e., the number of iterations required to reach convergence).

Appendix B. Linear System Coefficients

The discretised momentum equation for an arbitrary cell P is expressed by Equation (34), where the central (diagonal) and neighbour (off-diagonal) tensorial (3×3) coefficients associated with the unknown displacement increment field read as follows:

$$\mathbf{A}_P^{\delta \boldsymbol{u}} = \frac{\rho_P^0 \Omega_P^0}{(\Delta t)^2} \boldsymbol{I} + \sum_f \frac{(\mu_{\text{eff}})_f \Gamma_f^0}{d_{f,n}^0} \boldsymbol{I} + \sum_f \frac{(\mu_{\text{eff}})_f \Gamma_f^0 (\boldsymbol{nn})_f^0}{d_{f,n}^0}, \tag{A1}$$

$$\mathbf{A}_N^{\delta \boldsymbol{u}} = -\frac{(\mu_{\text{eff}})_f \Gamma_f^0}{d_{f,n}^0} \boldsymbol{I} - \frac{(\mu_{\text{eff}})_f \Gamma_f^0 (\boldsymbol{nn})_f}{d_{f,n}^0}. \tag{A2}$$

Corresponding vectorial (3×1) coefficients associated with the unknown pressure increment field read as follows:

$$\mathbf{A}_P^{\delta \boldsymbol{u}, \delta p} = \sum_f [(\boldsymbol{F}_f^n)^{-\mathrm{T}} \cdot \boldsymbol{n}_f^0] g_x^0 \Gamma_f^0, \tag{A3}$$

$$\mathbf{A}_N^{\delta \boldsymbol{u}, \delta p} = [(\boldsymbol{F}_f^n)^{-\mathrm{T}} \cdot \boldsymbol{n}_f^0] (1 - g_x^0) \Gamma_f^0. \tag{A4}$$

Finally, the right-hand side (source) vector in Equation (34) reads as follows:

$$\mathbf{r}_P^{\delta \boldsymbol{u}} = \frac{\rho_P^0 \boldsymbol{v}_P^n \Omega_P^0}{\Delta t} + \sum_f \boldsymbol{T}_f^n \Gamma_f^0 + \sum_f (\boldsymbol{T}_f')^* \Gamma_f^0 - \sum_f [(\boldsymbol{F}_f^n)^{-\mathrm{T}} \cdot \boldsymbol{n}_f^0] [\mathbf{k}_f^0 \cdot {}^0\overline{(\nabla_0 \delta p)}_f^*] \Gamma_f^0. \tag{A5}$$

The discretised incompressibility condition for an arbitrary cell P is expressed by Equation (39), where the central (diagonal) and neighbour (off-diagonal) scalar coefficients associated with the unknown pressure increment field read as follows:

$$A_P^{\delta p} = \sum_f \left[{}^m\overline{\left(\frac{A_P^{\delta \boldsymbol{u}}}{\Omega_P^0} \right)_f} \right]^{-1} \frac{\Gamma_f^m}{|\mathbf{d}_f^m|}, \tag{A6}$$

$$A_N^{\delta p} = -\left[{}^m\overline{\left(\frac{A_P^{\delta \boldsymbol{u}}}{\Omega_P^0} \right)_f} \right]^{-1} \frac{\Gamma_f^m}{|\mathbf{d}_f^m|}. \tag{A7}$$

The vectorial coefficients related to the unknown displacement increment field are as follows:

$$\mathbf{A}_P^{\delta p,\delta \boldsymbol{u}} = \sum_f \boldsymbol{n}_f^m g_x^m \Gamma_f^m, \tag{A8}$$

$$\mathbf{A}_N^{\delta p,\delta \boldsymbol{u}} = \boldsymbol{n}_f^m (1 - g_x^m) \Gamma_f^m, \tag{A9}$$

while the right-hand side term reads as follows:

$$\begin{aligned} r_P^{\delta p} = & \sum_f \boldsymbol{n}_f^m \cdot \left[\mathbf{k}_f^m \cdot {}^m\overline{(\nabla_m \delta \boldsymbol{u})}_f^* \right] \Gamma_f^m + \\ & \sum_f \left[{}^m\overline{\left(\frac{A_P^{\delta \boldsymbol{u}}}{\Omega_P^0} \right)}_f \right]^{-1} \widehat{\mathbf{d}}_f^m \cdot {}^m\overline{(\nabla_m \delta p)}_f^* \Gamma_f^m, \end{aligned} \tag{A10}$$

where $(\nabla_m \delta \boldsymbol{u})$ is the displacement increment gradient evaluated on the intermediate configuration corresponding to the time instance $t^m = t^{n+1/2}$.

Appendix C. Consistent Rhie–Chow Interpolation

In this work, the temporally consistent Rhie–Chow interpolation is achieved by adding an explicit correction term, $\delta\Omega_f^{\mathrm{CRC}}$, to the right-hand side of Equation (37). The derivation of this correction term follows the approach proposed in Bartholomew et al. [14], adjusted to the particular problem considered in this work. The final form of the correction term for the case of the Euler temporal discretisation scheme reads as follows:

$$\delta\Omega_f^{\mathrm{CRC}} = \frac{\rho_P^0}{\Delta t} \left[{}^m\overline{\left(\frac{A_P^{\delta \boldsymbol{u}}}{\Omega_P^0} \right)}_f \right]^{-1} \left[\boldsymbol{v}_f^n - {}^m\overline{\overline{(\boldsymbol{v}_P^n)}}_f \right] \cdot \boldsymbol{\Gamma}_f^{n+1/2}, \tag{A11}$$

where ${}^m\overline{\overline{(\boldsymbol{v}_P^n)}}_f$ is the cell-face velocity obtained by linear interpolation with skewness correction of the cell-center velocity, and $\boldsymbol{v}_f^n$ is the cell-face velocity calculated by taking the temporal derivative of the conservative cell-face displacement. The same procedure is used to derive the correction term for the remaining temporal discretisation schemes.

Appendix D. Material Laws

Appendix D.1. HGO Model

The Holzapfel–Gasser–Ogden (HGO) constitutive model is widely used to describe the nonlinear mechanical response of arterial tissue. In this implementation, the model is formulated with three material parameters and uses two families of collagen fibers. The fibers are assumed to be arranged symmetrically around the circumferential axis at angles $\pm\varphi$. They reinforce the isotropic matrix, making the tissue stiffer and highly anisotropic.

The strain energy density function is defined as follows:

$$\Psi = \Psi_{\mathrm{iso}} + \Psi_{\mathrm{aniso}} = \frac{\mu}{2}(I_1 - 3) + \frac{k_1}{2k_2} \sum_{i=4,6} \left(\exp\left[k_2 (I_i - 1)^2 \right] - 1 \right), \tag{A12}$$

where μ is the shear modulus of the isotropic ground matrix, k_1 and k_2 are material parameters associated with the collagen fibers, and I_1, I_4, and I_6 are strain invariants.

The invariants are computed as follows:

$$I_1 = \mathrm{tr}(\mathbf{C}), \quad I_4 = \mathbf{C} : (\mathbf{a}_0 \otimes \mathbf{a}_0), \quad I_6 = \mathbf{C} : (\mathbf{b}_0 \otimes \mathbf{b}_0), \tag{A13}$$

where $\mathbf{C} = \mathbf{F}^{\mathrm{T}}\mathbf{F}$ is the right Cauchy–Green deformation tensor, and $\mathbf{a}_0$, $\mathbf{b}_0$ are unit vectors in the reference configuration defining the preferred fiber directions.

The corresponding Cauchy stress tensor is obtained as follows:

$$\begin{aligned}\sigma = &-p\,\mathbf{I} + \mu(\mathbf{B} - \mathbf{I}) \\ &+ 2k_1(I_4 - 1)\,exp\big[k_2(I_4 - 1)^2\big]\,(\mathbf{a}\otimes\mathbf{a}) \\ &+ 2k_1(I_6 - 1)\,\exp\big[k_2(I_6 - 1)^2\big]\,(\mathbf{b}\otimes\mathbf{b})\,.\end{aligned} \tag{A14}$$

Appendix D.2. Guccione Model

To describe the mechanical behaviour of cardiac tissue, the Guccione constitutive model was implemented. This model takes into account the presence of collagen fibers, which reinforce the tissue matrix and contribute to its stiffness and strength. As a result, the tissue exhibits anisotropic behaviour, specifically transverse isotropy, due to the directional alignment of fibers.

The strain energy density function Ψ is defined as follows:

$$\Psi = \frac{k}{2}(e^Q - 1) \tag{A15}$$

where k is a material constant and Q is a scalar function representing the anisotropic response of the tissue, given by the following:

$$Q = b_t I_1^2 - 2b_t I_2 + (b_f - 2b_{fs} + b_t)I_4^2 + 2(b_{fs} - b_t)I_5 \tag{A16}$$

Here, b_t, b_f, and b_{fs} are material parameters, and I_1, I_2, I_4, and I_5 are invariants of the Green–Lagrange strain tensor $\mathbf{C}$. The Green-Lagrange strain is computed from the deformation gradient $\mathbf{F}$ as follows:

$$\mathbf{C} = \frac{1}{2}(\mathbf{F}^T \cdot \mathbf{F} - \mathbf{I}) \tag{A17}$$

with the deformation gradient defined as follows:

$$\mathbf{F} = \mathbf{I} + \frac{\partial \mathbf{u}}{\partial \mathbf{X}} \tag{A18}$$

where $\mathbf{u}$ is the displacement vector and $\mathbf{X}$ is the reference configuration. The strain invariants are computed as follows:

$$I_1 = \mathrm{tr}(\mathbf{C}), \quad I_2 = \frac{1}{2}\Big[(\mathrm{tr}(\mathbf{C}))^2 - \mathrm{tr}(\mathbf{C}\cdot\mathbf{C})\Big], \quad I_4 = \mathbf{C} : (\mathbf{f}_0 \otimes \mathbf{f}_0), \quad I_5 = \mathbf{C^2} : (\mathbf{f}_0 \otimes \mathbf{f}_0), \tag{A19}$$

where f_0 is a unit vector of reference fiber direction.

The second Piola–Kirchhoff stress tensor $\mathbf{S}$ is then obtained by differentiating the strain energy density with respect to $\mathbf{C}$:

$$S = \frac{\partial \Psi}{\partial \mathbf{C}} = \frac{\partial Q}{\partial \mathbf{C}}\frac{k}{2}e^Q \tag{A20}$$

The derivative of Q with respect to the Green-Lagrange strain $\frac{\partial Q}{\partial \mathbf{C}}$ is as follows:

$$\frac{\partial Q}{\partial \mathbf{C}} = 2c_t\mathbf{C} + 2(b_f - 2b_{fs} + b_t)I_4(f_0 \otimes f_0) + 2(b_{fs} - b_t)(\mathbf{C}(\cdot f_0 \otimes f_0) + (f_0 \otimes f_0)\cdot\mathbf{C})) \tag{A21}$$

Appendix E. Pressurised Cylinder Equations

The strain energy density Ψ for an incompressible neo-Hookean material is as follows:

$$\Psi = \frac{1}{2}\mu(I_1 - 3) \tag{A22}$$

where μ is the shear modulus. From the strain energy density function Equation (A22), the Cauchy stress from can be written as follows:

$$\boldsymbol{\sigma} = -p\boldsymbol{I} + \mu\boldsymbol{b} \tag{A23}$$

The loading case and the geometry of the cylinder are shown on Figure 15 in the reference configuration in a $\frac{1}{4}$-section view. Based on this, the current configuration coordinates can be defined with respect to the reference configuration ones:

$$r = f(R), \quad \theta = \Theta, \quad z = \lambda Z \tag{A24}$$

where λ is the axial stretch of the cylinder. The deformation gradient tensor can then be written as follows:

$$\boldsymbol{F} = \begin{bmatrix} \lambda_r & & \\ & \lambda_\theta & \\ & & \lambda_z \end{bmatrix} = \begin{bmatrix} \frac{dr}{dR} & & \\ & \frac{r}{R} & \\ & & \lambda \end{bmatrix} \tag{A25}$$

hence, the stretches are as follows:

$$\lambda_r = \frac{dr}{dR}, \quad \lambda_\theta = \frac{r}{R}, \quad \lambda_z = \lambda \tag{A26}$$

but considering that the material is incompressible, $J = \det \boldsymbol{F} = \lambda_1\lambda_2\lambda_3 = 1$ that the radial stretch is as follows:

$$\lambda_r = \frac{dr}{dR} = \frac{J}{\lambda_\theta \lambda_z} = \frac{R}{\lambda r} \tag{A27}$$

By using Equations (A25)–(A27) the left Cauchy-Green tensor $\boldsymbol{b} = \boldsymbol{F}\boldsymbol{F}^{\mathrm{T}}$ can be written as follows:

$$\boldsymbol{b} = \begin{bmatrix} \left(\frac{R}{\lambda r}\right)^2 & & \\ & \left(\frac{r}{R}\right)^2 & \\ & & \lambda^2 \end{bmatrix} \tag{A28}$$

while the components of the Cauchy stress tensor from Equation (A23) become:

$$\begin{aligned} \sigma_{rr} &= -p + \mu\left(\frac{R}{\lambda r}\right)^2 \\ \sigma_{\theta\theta} &= -p + \mu\left(\frac{r}{R}\right)^2 \\ \sigma_{zz} &= -p + \mu\lambda^2 \end{aligned} \tag{A29}$$

The equilibrium equation is as follows:

$$\nabla \cdot \boldsymbol{\sigma} = \boldsymbol{0} \tag{A30}$$

which, when combined with Equation (A29), leaves only the radial component as the non-trivial solution:

$$\frac{d\sigma_{rr}}{dr} + \frac{1}{r}(\sigma_{rr} - \sigma_{\theta\theta}) = 0 \tag{A31}$$

with the following boundary conditions

$$\sigma_{rr}|_a = -p, \quad \sigma_{rr}|_b = 0 \tag{A32}$$

where a and b are the inner and outer radii of the cylinder in the current configuration, respectively. Similarly, A and B are the inner and outer radii of the cylinder in the reference configuration.

By integrating Equation (A27) from the internal surface up to some radius:

$$\int_a^r \lambda r dr = \int_A^R R dR$$

the current and reference configuration radii can be written as functions of one another:

$$r = \left[a^2 + \frac{R^2 - A^2}{\lambda}\right]^{\frac{1}{2}}, \quad R = \left[\lambda\left(r^2 - a^2\right) + A^2\right]^{\frac{1}{2}} \tag{A33}$$

By using Equation (A33), the stretches from Equation (A26) can be rewritten as functions of the reference configuration radius:

$$\begin{aligned} \lambda_r &= \frac{R}{\lambda r} = \frac{R}{\lambda}\left[a^2 + \frac{R^2 - A^2}{\lambda}\right]^{-\frac{1}{2}} \\ \lambda_\theta &= \frac{r}{R} = \frac{1}{R}\left[a^2 + \frac{R^2 - A^2}{\lambda}\right]^{\frac{1}{2}} \\ \lambda_z &= \lambda \end{aligned} \tag{A34}$$

By integrating Equation (A31) from the internal to the external surface, the following is obtained:

$$\int_{-p}^{0} d\sigma_{rr} = \int_a^b \frac{1}{r}(\sigma_{\theta\theta} - \sigma_{rr}) dr = \mu \int_a^b \frac{1}{r}\left[\left(\frac{r}{R}\right)^2 - \left(\frac{R}{\lambda r}\right)^2\right] dr = p \tag{A35}$$

and by using Equation (A33), after some rearranging, this becomes the following:

$$p = \frac{\mu}{\lambda}\ln\left(\frac{B}{A}\right) - \frac{\mu}{2\lambda}\ln\left(\frac{\lambda a^2 + B^2 - A^2}{\lambda^2 a^2}\right) - \frac{\mu\left(\lambda a^2 - A^2\right)}{2\lambda\left(\lambda a^2 + B^2 - A^2\right)} + \frac{\mu\left(\lambda a^2 - A^2\right)}{2\lambda^2 a^2} \tag{A36}$$

For practical reasons, define the variable ζ as follows:

$$\zeta = \lambda a^2 + B^2 - A^2, \quad \frac{d\zeta}{da} = 2\lambda a \tag{A37}$$

Now using Equation (A37), Equation (A36) becomes the following:

$$p = \frac{\mu}{\lambda}\ln\left(\frac{B}{A}\right) - \frac{\mu}{2\lambda}\ln\left(\frac{\zeta}{\lambda^2 a^2}\right) - \frac{\mu\left(\zeta - B^2\right)}{2\lambda\zeta} + \frac{\mu\left(\zeta - B^2\right)}{2\lambda^2 a^2} \tag{A38}$$

Hence, by prescribing the inner radius in the current configuration and the axial stretch λ, the loading pressure can be computed from Equation (A38), assuming that the reference geometry of the cylinder is known, i.e., A and B.

Usually, though, the loading pressure p is known, and the geometry in the current configuration needs to be computed. If the inner radius in the current configuration is known, then it is easy to compute various other values (e.g., the deformed outer radius and the stress distribution). Consequently, Equation (A38) can be used to compute the deformed inner radius if the loading pressure is known.

Using Equation (A38), define the function:

$$f(a) = p - \frac{\mu}{\lambda}\ln\left(\frac{B}{A}\right) + \frac{\mu}{2\lambda}\ln\left(\frac{\zeta}{\lambda^2 a^2}\right) + \frac{\mu\left(\zeta - B^2\right)}{2\lambda\zeta} - \frac{\mu\left(\zeta - B^2\right)}{2\lambda^2 a^2} = 0 \tag{A39}$$

by solving Equation (A39) for a given geometry, loading pressure, and axial stretch, the deformed internal radius a is obtained. This can be done by employing any number of methods, for example, the Newton's method, for which the derivative of $f(a)$ is required:

$$\frac{df(a)}{da} = \frac{\mu a}{\zeta} + \frac{\mu a B^2}{\zeta^2} + \frac{\mu\left(\zeta - B^2\right)}{\lambda^2 a^3} - \frac{2\mu}{\lambda a} \tag{A40}$$

The distribution of the radial component of the Cauchy stress can be obtained by integrating Equation (A31) from the internal surface up to some arbitrary radius:

$$\int_p^{\sigma_{rr}} d\sigma_{rr} = \int_a^r \frac{1}{r}(\sigma_{\theta\theta} - \sigma_{rr})dr = \mu\int_a^r \frac{1}{r}\left[\left(\frac{r}{R}\right)^2 - \left(\frac{R}{\lambda r}\right)^2\right]dr = \sigma_{rr} - p \tag{A41}$$

which, upon further integration and after some rearranging yields the following:

$$\sigma_{rr}(r) = -p + \frac{\mu}{2\lambda}\left[\ln\left(\frac{\lambda r^2 - \lambda a^2 + A^2}{A^2}\right) - \ln\left(\frac{r}{a}\right)^2 - \frac{\left(\lambda a^2 - A^2\right)\left(a^2 - r^2\right)}{\lambda r^2 a^2}\right] \tag{A42}$$

note that p in Equation (A42) refers to the internal loading pressure. Also note that by using Equation (A33), Equation (A42) can be expressed in terms of the reference configuration radius.

The radial hydrostatic pressure distribution can be obtained by combining Equations (A42) and (A33) with Equation (A29), which yields the following:

$$p(r) = \mu\frac{\lambda r^2 - \lambda a^2 + A^2}{\lambda^2 r^2} - \sigma_{rr}(r) \tag{A43}$$

References

1. Sussman, T.; Bathe, K.J. A finite element formulation for nonlinear incompressible elastic and inelastic analysis. *Comput. Struct.* **1987**, *26*, 357–409. [CrossRef]
2. Cardiff, P.; Demirdžić, I. Thirty Years of the Finite Volume Method for Solid Mechanics. *Arch. Comput. Methods Eng.* **2021**, *28*, 3721–3780. [CrossRef]
3. Wheel, M.A. A mixed finite volume formulation for determining the small strain deformation of incompressible materials. *Int. J. Numer. Methods Eng.* **1999**, *44*, 1843–1861. [CrossRef]
4. Bijelonja, I.; Demirdžić, I.; Muzaferija, S. A finite volume method for large strain analysis of incompressible hyperelastic materials. *Int. J. Numer. Methods Eng.* **2005**, *64*, 1594–1609. [CrossRef]
5. Bijelonja, I.; Demirdžić, I.; Muzaferija, S. A finite volume method for incompressible linear elasticity. *Comput. Methods Appl. Mech. Eng.* **2006**, *195*, 6378–6390. [CrossRef]
6. Bijelonja, I.; Demirdžić, I.; Muzaferija, S. Mixed finite volume method for linear thermoelasticity at all Poisson's ratios. *Numer. Heat Transf. Part A Appl.* **2017**, *72*, 215–235. [CrossRef]

7. Patankar, S.; Spalding, D. A calculation procedure for heat, mass and momentum transfer in three-dimensional parabolic flows. *Int. J. Heat Mass Transf.* **1972**, *15*, 1787–1806. [CrossRef]
8. Rhie, C.M.; Chow, W.L. Numerical study of the turbulent flow past an airfoil with trailing edge separation. *AIAA J.* **1983**, *21*, 1525–1532. [CrossRef]
9. Darwish, M.; Sraj, I.; Moukalled, F. A coupled finite volume solver for the solution of incompressible flows on unstructured grids. *J. Comput. Phys.* **2009**, *228*, 180–201. [CrossRef]
10. Mangani, L.; Alloush, M.M.; Lindegger, R.; Hanimann, L.; Darwish, M. A Pressure-Based Fully-Coupled Flow Algorithm for the Control Volume Finite Element Method. *Appl. Sci.* **2022**, *12*, 4633. [CrossRef]
11. Uroić, T.; Jasak, H. Block-selective algebraic multigrid for implicitly coupled pressure-velocity system. *Comput. Fluids* **2018**, *167*, 100–110. [CrossRef]
12. Fernandes, C.; Vukčević, V.; Uroić, T.; Simoes, R.; Carneiro, O.; Jasak, H.; Nóbrega, J. A coupled finite volume flow solver for the solution of incompressible viscoelastic flows. *J. Non-Newton. Fluid Mech.* **2019**, *265*, 99–115. [CrossRef]
13. Weller, H.G.; Tabor, G.; Jasak, H.; Fureby, C. A tensorial approach to computational continuum mechanics using object-oriented techniques. *Comput. Phys.* **1998**, *12*, 620–631. [CrossRef]
14. Bartholomew, P.; Denner, F.; Abdol-Azis, M.H.; Marquis, A.; van Wachem, B.G. Unified formulation of the momentum-weighted interpolation for collocated variable arrangements. *J. Comput. Phys.* **2018**, *375*, 177–208. [CrossRef]
15. Holzapfel, G.A.; Gasser, T.C.; Ogden, R.W. A new constitutive framework for arterial wall mechanics and a comparative study of material models. *J. Elast.* **2000**, *61*, 1–48. [CrossRef]
16. Guccione, J.M.; McCulloch, A.D.; Waldman, L.K. Passive material properties of intact ventricular myocardium determined from a cylindrical model. *J. Biomech. Eng.* **1991**, *113*, 42–55. [CrossRef]
17. Cardiff, P.; Karač, A.; De Jaeger, P.; Jasak, H.; Nagy, J.; Ivanković, A.; Tuković, Ž. An open-source finite volume toolbox for solid mechanics and fluid-solid interaction simulations. *arXiv* **2018**, arXiv.1808.10736. [CrossRef]
18. Cardiff, P.; Batistić, I.; Tuković, Ž. solids4foam: A toolbox for performing solid mechanics and fluid-solid interaction simulations in OpenFOAM. *J. Open Source Softw.* **2025**, *10*, 7407. [CrossRef]
19. Demirdžić, I.; Cardiff, P. Symmetry plane boundary conditions for cell-centred finite-volume continuum mechanics. *Numer. Heat Transf. Part B Fundam.* **2022**, *83*, 12–23. [CrossRef]
20. Greco, M.; Peixoto, D.H.N. Comparative assessments of strain measures for nonlinear analysis of truss structures at large deformations. *Eng. Comput.* **2021**, *39*, 1621–1641. [CrossRef]
21. Peixoto, D.H.N.; Greco, M.; Vasconcellos, D.B. A new family of strain tensors based on the hyperbolic sine function. *Lat. Am. J. Solids Struct.* **2024**, *21*, 529. [CrossRef]
22. Vasconcellos, D.B.; Greco, M. Reconciling the strain-stretching curve with the stress-strain diagram of a Hooke-like isotropic hyperelastic material using the Biot's hyperbolic sine strain tensor. *Lat. Am. J. Solids Struct.* **2025**, *22*, 8362. [CrossRef]
23. Tuković, Ž.; Karač, A.; Cardiff, P.; Jasak, H.; Ivanković, A. OpenFOAM Finite Volume Solver for Fluid-Solid Interaction. *Trans. FAMENA* **2018**, *42*, 1–31. [CrossRef]
24. Bathe, K.J.; Baig, M.M.I. On a composite implicit time integration procedure for nonlinear dynamics. *Comput. Struct.* **2005**, *83*, 2513–2524. [CrossRef]
25. Bathe, K.J.; Noh, G.C. Insight into an implicit time integration scheme for structural dynamics *Comput. Struct.* **2012**, *98–99*, 1–6. [CrossRef]
26. Tuković, Ž.; Perić, M.; Jasak, H. Consistent second-order time-accurate non-iterative PISO-algorithm. *Comput. Fluids* **2018**, *166*, 78–85. [CrossRef]
27. Demirdžić, I.; Muzaferija, S. Numerical method for coupled fluid flow, heat transfer and stress analysis using unstructured moving meshes with cells of arbitrary topology. *Comput. Methods Appl. Mech. Eng.* **1995**, *125*, 235–255. [CrossRef]
28. Maas, S.A.; Ellis, B.J.; Ateshian, G.A.; Weiss, J.A. FEBio: Finite Elements for Biomechanics. *J. Biomech. Eng.* **2012**, *134*. [CrossRef]
29. Maas, S.A.; Ateshian, G.A.; Weiss, J.A. FEBio: History and Advances. *Annu. Rev. Biomed. Eng.* **2017**, *19*, 279–299. [CrossRef]
30. Timoshenko, S.; Goodier, J. *Theory of Elasticity*; McGraw-Hill Book Company: Columbus, OH, USA, 1970.
31. Land, S.; Gurev, V.; Arens, S.; Augustin, C.M.; Baron, L.; Blake, R.; Bradley, C.; Castro, S.; Crozier, A.; Favino, M.; et al. Verification of cardiac mechanics software: Benchmark problems and solutions for testing active and passive material behaviour. *Proc. R. Soc. A Math. Phys. Eng. Sci.* **2015**, *471*, 20150641. [CrossRef]
32. Fridez, P.; Makino, A.; Miyazaki, H.; Meister, J.; Hayashi, K.; Stergiopulos, N. Short-Term biomechanical adaptation of the rat carotid to acute hypertension: Contribution of smooth muscle. *Ann. Biomed. Eng.* **2001**, *29*, 26–34. [CrossRef] [PubMed]

33. Zulliger, M.A.; Fridez, P.; Hayashi, K.; Stergiopulos, N. A strain energy function for arteries accounting for wall composition and structure. *J. Biomech.* **2004**, *37*, 989–1000. [CrossRef]
34. Sun, W.; Chaikof, E.L.; Levenston, M.E. Numerical Approximation of Tangent Moduli for Finite Element Implementations of Nonlinear Hyperelastic Material Models. *J. Biomech. Eng.* **2008**, *130*, 061003. [CrossRef]

Disclaimer/Publisher's Note: The statements, opinions and data contained in all publications are solely those of the individual author(s) and contributor(s) and not of MDPI and/or the editor(s). MDPI and/or the editor(s) disclaim responsibility for any injury to people or property resulting from any ideas, methods, instructions or products referred to in the content.